Inorganic Chemistry
Article
Cite This: Inorg. Chem. 2019, 58, 12756−12774
pubs.acs.org/IC

The Influence of Redox-Innocent Donor Groups in Tetradentate Ligands Derived from *o*-Phenylenediamine: Electronic Structure Investigations with Nickel

Kyle D. Spielvogel,[†] Ezra J. Coughlin,[§] Hayley Petras,[†] Javier A. Luna,[†] Austin Benson,[†] Courtney M. Donahue,[†] Amani Kibasa,[†] Kyounghoon Lee,[†] Ryan Salacinski,[†] Suzanne C. Bart,[§] Scott K. Shaw,*[,†] James J. Shepherd,*[,†] and Scott R. Daly*[,†]

[†]Department of Chemistry, The University of Iowa, E331 Chemistry Building, Iowa City, Iowa 52242-1294, United States
[§]H.C. Brown Laboratory, Department of Chemistry, Purdue University, West Lafayette, Indiana 47907, United States

Supporting Information

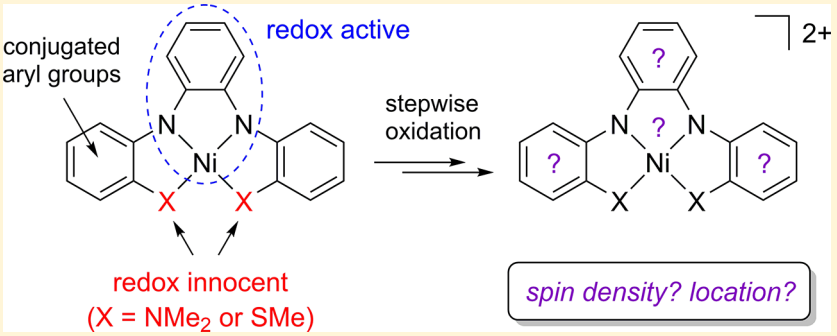

ABSTRACT: The continued development of redox-active ligands requires an understanding as to how ligand modifications and related factors affect the locus of redox activity and spin density in metal complexes. Here we describe the synthesis, characterization, and electronic structure of nickel complexes containing triaryl NNNN (**1**) and SNNS (**2**) ligands derived from *o*-phenylenediamine. The tetradentate ligands in **1** and **2** were investigated and compared to those in metal complexes with compositionally similar ligands to determine how ligand-centered redox properties change when redox-active flanking groups are replaced with redox-innocent NMe_2 or SMe. A derivative of **2** in which the phenylene backbone was replaced with ethylene (**3**) was also prepared to interrogate the importance of *o*-phenylenediamine for ligand-centered redox activity. Cyclic voltammograms collected for **1** and **2** revealed two fully reversible ligand-centered redox events. Remarkably, several quasi-reversible ligand-centered redox waves were also observed for **3** despite the absence of the *o*-phenylenediamine subunit. Oxidizing **1** and **2** with silver salts containing different counteranions (BF_4^-, OTf^-, NTf_2^-) allowed the electrochemically generated complexes to be analyzed as a function of different oxidation states using single-crystal X-ray diffraction (XRD), EPR spectroscopy, and S K-edge X-ray absorption spectroscopy. The experimental data are corroborated by DFT calculations, and together, they reveal how the location of unpaired spin density and electronic structure in singly and doubly oxidized salts of **1** and **2** varies depending on the coordinating ability of the counteranions and exogenous ligands such as pyridine.

INTRODUCTION

Metal complexes with redox-active ligands are renowned for their ability to enable and promote new types of reactivity,[1,2] especially with metals that prefer to undergo one-electron redox transformations or display limited redox activity on their own. Given their crucial role in mediating electron-transfer reactions in metalloproteins and their prominent use in the development of homogeneous catalysts with earth abundant metals,[3−13] understanding how redox-active ligand modifications affect the electronic structure and reactivity of metal complexes remains an important goal.

o-Phenylenediamine is a classic redox-active ligand. While bound to metals, it can undergo two reversible one-electron oxidations to form the *o*-diiminosemiquinone radical followed by the fully oxidized *o*-diiminoquinone (Chart 1).[14] Since the pioneering work of Holm[15,16] and important electronic structure investigations by Wieghardt,[17] *o*-phenylenediamine has been incorporated into conjugated multidentate ligands as

Chart 1. One-Electron Redox Transformations with *o*-Phenylenediamine

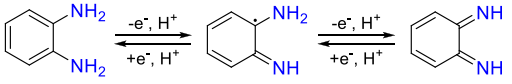

Received: June 5, 2019
Published: September 6, 2019

DOI: 10.1021/acs.inorgchem.9b01675
Inorg. Chem. 2019, 58, 12756−12774

a means to tune ligand redox properties, improve complex stability, and accommodate different metal coordination environments. This is perhaps most well-known with tetradentate salophen ligands,[18,19] but another approach is to use direct N-aryl linkages to access additional ligand-centered redox transformations and alter the locus of ligand-centered redox events. For example, Wieghardt and co-workers showed that square planar Cu(II) and Zn(II) complexes with triaryl ONNO ligands undergo ligand-centered redox reactions that involve both the *o*-phenylenediamine backbone and the flanking phenolate arms (Chart 2).[17] In contrast, Thomas and co-workers more recently reported that isostructural Ni(II) NNNN complexes with flanking aniline groups undergo four redox transformations that localize on the aniline groups.[20]

Chart 2. Triaryl Tetradentate Ligands Described Previously and Abbreviations for Ligands Reported Here

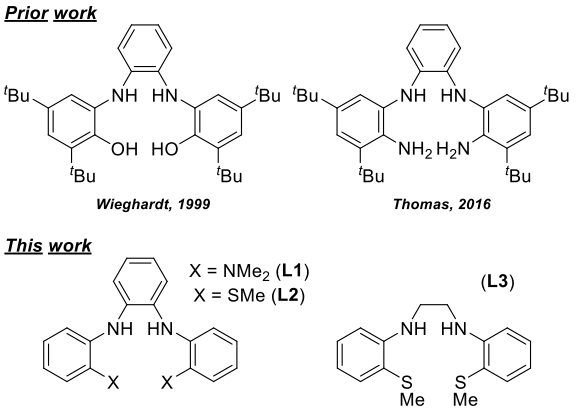

Flanking OH and NH_2 donor substituents in triaryl tetradentate ligands, as shown in Chart 2, are considered noninnocent because they actively participate in redox transformations with concomitant proton loss and change in O or N hybridization. We recently began investigating how replacing these flanking donors with redox-inactive (i.e., redox-innocent) substituents alters ligand-centered redox activity. We postulated that redox-innocent donor groups would help direct redox activity to the *o*-phenylenediamine backbone, which is desirable for our efforts to understand how metal−ligand cooperativity (MLC) across metal−nitrogen bonds affects redox activity at the ligand and metal. However, our previous MLC studies with ruthenium complexes containing the $H_2(^{Me}SNNS^{Me})$-DAB ligand (**L2**, Chart 2) yielded redox waves in the cyclic voltammograms that were difficult to assign based on comparison to electrochemical data reported for similar systems.[21−24] These difficulties stemmed in part from the fact that ruthenium has a Ru^{3+}/Ru^{2+} redox couple that can fall within the range of redox potentials expected for *o*-phenylenediamine ligands.[21−24] Moreover, ruthenium 4d orbitals are often highly delocalized with frontier π orbitals of *o*-phenylenediamine and related redox-active ligands,[25,26] which further complicates redox assignments and interpretation. It has also been shown that thioethers can be redox-noninnocent in different ligand frameworks such as thioether crowns,[27−29] which has raised questions as to whether the thioether substituents in **L2** are indeed redox-innocent. However, as we will show, the thioether substituents in **L2** do not appear to be participating in the ligand-centered redox events.

To simplify our electrochemical investigations and help identify the locus of ligand-centered redox activity, we prepared a series of Ni(II) complexes with the aforementioned SNNS ligand **L2**, as well as a new triaryl tetradentate ligand containing flanking NMe_2 substituents (**L1**; Chart 2). Nickel was selected because it does not have readily accessible redox couples to interfere with assignments in our electrochemical window of interest, and the more contracted 3d orbitals on nickel are expected to delocalize less into the π manifold of redox-active ligands relative to 4d orbitals on ruthenium. The tetradentate ligand $H_2(^{Me}NNNN^{Me})$-DAB (**L1**) was prepared and investigated alongside our previously reported $H_2(^{Me}SNNS^{Me})$-DAB ligand (**L2**) to compare substituents with different hard/soft donor strength, evaluate potential differences in redox noninnocence, and provide a more direct comparison to the NNNN complexes described by Thomas et al.[20] While dithiolate SNNS complexes without the *o*-phenylenediamine subunit are known with Ni,[30] we are not aware of any examples with similar triaryl ligands and flanking thiol substituents to evaluate against our thioether-substituted ligand **L2**. Finally, to investigate the importance of the *o*-phenylenediamine backbone for ligand-centered redox activity, we prepared a known derivative of the SNNS ligand **L2** in which the phenylene backbone was replaced with an ethylene linker (**L3**; Chart 2). Here we present our synthetic results alongside comparative X-ray diffraction data, electrochemical studies, spectroscopic analyses, and density functional theory (DFT) calculations to elucidate the electronic structure of these complexes as a function of differing oxidation states, ligand modifications, and coordinating ancillary ligands.

RESULTS AND DISCUSSION

Synthesis and Characterization of Ni(II) Complexes. The triaryl $H_2(^{Me}NNNN^{Me})$-DAB ligand (**L1**) was prepared by palladium-catalyzed Buchwald−Hartwig cross-coupling of *o*-phenylenediamine with 2 equiv of 2-bromo-*N*,*N*′-dimethylaniline, using a procedure similar to that described for the $H_2(^{Me}SNNS^{Me})$-DAB ligand (**L2**).[31] **L1** was isolated in 62% yield after purification by column chromatography and subsequent crystallization. ^1H and ^{13}C NMR spectroscopy, electron impact mass spectrometry (EI-MS), microanalysis, infrared spectroscopy, and single-crystal X-ray diffraction (XRD) confirmed the identity of **L1**. The chemically equivalent NMe_2 groups appeared as a singlet in the ^1H and ^{13}C NMR spectra at δ 2.58 and 44.16 ppm, respectively, and

Scheme 1. Syntheses and Structures of 1−3

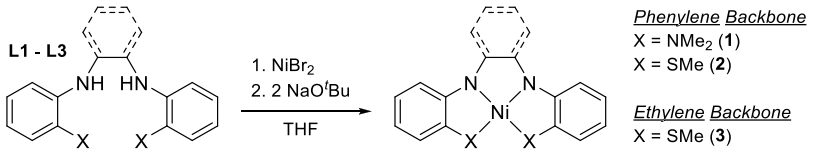

DOI: 10.1021/acs.inorgchem.9b01675
Inorg. Chem. 2019, 58, 12756−12774

Table 1. Selected Bond Distances (Å) and Angles (deg) from Single-Crystal XRD Data[a]

	1	1[BF_4]	1[OTf]$_2$	2	2[BF_4]	2[NTf_2]$_2$	2[OTf]$_2$	3
Ni−N1	1.830(3)	1.853(3)	2.002(3)	1.847(4)	1.914(6)	1.872(2)	2.005(3)	1.845(7)
Ni−N2	1.843(4)	1.845(3)	1.992(2)	1.845(4)	1.791(5)	1.871(2)	2.000(3)	1.850(7)
Ni−X1	2.025(4)	1.981(3)	2.112(2)	2.156(2)	2.081(2)	2.1933(7)	2.3787(9)	2.183(2)
Ni−X2	1.989(3)	2.008(3)	2.120(3)	2.149(1)	2.240(2)	2.1880(6)	2.391(1)	2.176(3)
Ni−O			2.160(2)			2.847(3)	2.147(2)	
			2.145(2)			2.794(2)	2.069(2)	
C1−C2	1.433(6)	1.449(4)	1.512(4)	1.414(8)	1.45(1)	1.484(3)	1.505(5)	1.54(1)
N1−C1	1.392(6)	1.359(4)	1.309(3)	1.401(6)	1.311(7)	1.321(3)	1.307(5)	1.44(1)
N2−C2	1.392(5)	1.354(4)	1.306(3)	1.400(6)	1.37(1)	1.327(3)	1.307(5)	1.45(1)
N1−C11	1.380(6)	1.401(4)	1.406(3)	1.384(7)	1.380(9)	1.413(3)	1.402(5)	1.37(1)
N2−C21	1.383(5)	1.400(4)	1.400(3)	1.376(7)	1.42(1)	1.415(3)	1.405(5)	1.35(1)
N−Ni−N	84.5(1)	84.2(1)	81.18(9)	86.2(2)	86.1(2)	84.12(8)	80.7(1)	85.2(3)
X−Ni−X	105.4(1)	104.8(1)	112.42(9)	96.95(6)	99.61(8)	97.47(2)	109.82(3)	97.2(1)

[a]X = SMe or NMe_2. All crystal structures follow the labeling scheme shown in Figure 1.

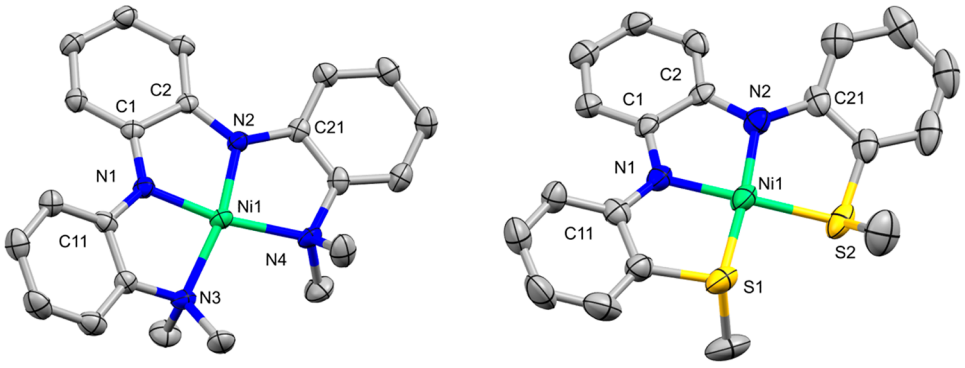

Figure 1. Molecular structures of **1** (left) and **2** (right) from single-crystal XRD studies. Ellipsoids are drawn at the 50% probability level. Hydrogen atoms were omitted from the figure.

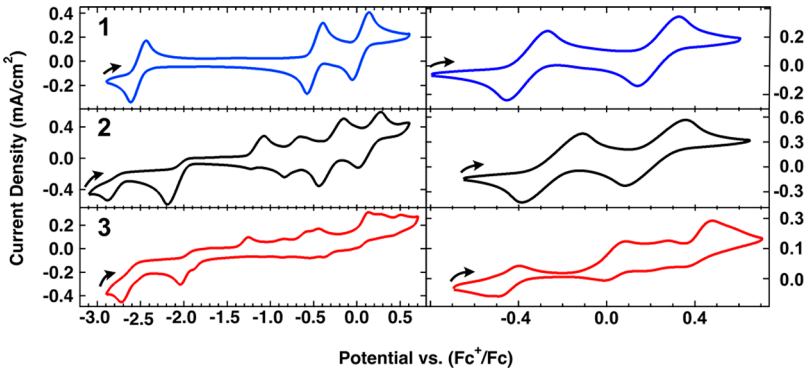

Figure 2. CV traces collected on 1 mM solutions of **1**−**3** in THF at 100 mV/s scan rates at room temperature with 0.1 M $TBAPF_6$. WE = glassy carbon, CE = Pt wire, RE = quasi Pt. (left) Scans collected out to ca. −3 V vs Fc^+/Fc. (right) CV scans collected with a truncated electrochemical window. Arrows signify the initial scan start point and scan direction.

the exchangeable N−H proton resonance was observed as a broad resonance in the ^{1}H NMR spectrum at δ 6.65 ppm. The remaining peak positions and integrations supported the triaryl framework of the ligand. The SNNS congener of **L2** in which the phenylene backbone is replaced with an ethylene linker—referred to here as H_2(^{Me}SNNS^{Me})-DAE (**L3**)—was prepared using a modified procedure reported by Bayer and Breitmaier.[32]

The Ni(II) complexes **1**−**3** were prepared by refluxing a 1:1 mixture of the corresponding ligand (**L1**−**L3**) and $NiBr_2$ in THF overnight (Scheme 1). In the absence of base, each reaction yielded a light green precipitate that was not characterized further due to its insolubility in organic solvents. Addition of 2 equiv of NaO^{t}Bu to the green precipitate, however, resulted in color changes over the course of 12 h to yield dark brown Ni(^{Me}NNNN^{Me})-DAB (**1**), dark green Ni(^{Me}SNNS^{Me})-DAB (**2**), and dark blue Ni(^{Me}SNNS^{Me})-DAE (**3**), respectively. All three compounds were crystallized in moderate yields (54−60%), and their formulation was confirmed by elemental analysis and NMR spectroscopy. The ^{1}H and ^{13}C NMR spectra for **1** in THF-D_8 revealed singlets for the chemically equivalent NMe_2 substituents at δ 3.05 and 50.34 ppm. The ^{1}H NMR resonances for the SMe substituents in **2** and **3** appeared more upfield at δ 1.71 and 1.87 ppm,

DOI: 10.1021/acs.inorgchem.9b01675
Inorg. Chem. 2019, 58, 12756−12774

Table 2. Redox Potentials of 1−3[a]

		Ni features		ligand features		
1	potential	−2.52[b]		−0.36[b]	0.23[b]	
	ΔE peak	0.18		0.18	0.18	
2	potential	−2.87[c]	−2.18[c]	−0.19[b]	0.22[b]	
	ΔE peak	irreversible	irreversible	0.28	0.27	
3	potential	−2.72[c]	−2.04[c]	−0.39[d]	0.08[d]	0.47[d]
	ΔE peak	irreversible	irreversible	irreversible	irreversible	irreversible

[a]CV traces collected on 1 mM solutions in THF at 100 mV/s scan rates at room temperature with 0.1 M $TBAPF_6$. WE = glassy carbon, CE = Pt wire, RE = quasi Pt. ΔE values are reported for reversible features (for comparison, ΔE = 0.21 V for Fc^+/Fc). All potentials and ΔE values are expressed in V and referenced to Fc^+/Fc. [b]Reported as $E_{1/2}$ for reversible waves. [c]Reported as E_{pc}. [d]Reported as E_{pa}.

respectively. While different stereoisomers of **2** and **3** are expected based on the possible orientations of the two SMe groups,[31] they could not be discerned presumably due to rapid exchange on the NMR time scale. The ^{13}C NMR spectra for **2** and **3** also revealed broadened resonances for the SMe groups at δ 24.16 and δ 24.56 ppm, respectively.

Single-crystal XRD studies revealed the anticipated square planar coordination geometries for all three complexes in the solid state. Selected bond distances and angles are presented in Table 1. The Ni−N bond distances range from 1.830(3) to 1.850(7) Å, consistent with covalent Ni−N bond distances reported previously with anionic amido ligands with flanking aryl substituents.[20,33,34] The Ni−SMe and Ni−NMe_2 distances also fall within their expected ranges at 2.149(1)−2.183(2) and 1.989(3)−2.025(4) Å, respectively.[35,36] Bond distances associated with the ligand will be discussed below with the structures of the chemically oxidized complexes (*vide infra*).

Electrochemical Studies. Cyclic voltammograms (CVs) of **1**−**3** were collected in THF to determine how changes in the neutral donor atoms (NMe_2 in **1** vs SMe in **2**) and backbone linker (phenylene in **2** vs ethylene in **3**) affect the redox chemistry of the Ni complexes (Figure 2). CVs of **1** and **2** were also collected in DCM (the solvent used for EPR studies below), and the results were consistent with those obtained in THF (Figures S52 and S53, Supporting Information). The CV of NMe_2-substituted **1** shows three fully reversible one-electron redox events with $E_{1/2}$ values of 0.23, −0.36, and −2.52 V vs Fc^+/Fc. The most negative wave at −2.52 V is assigned as the Ni^{2+}/Ni^{1+} redox couple based on comparison to literature reports.[35,37−40] The two waves at −0.36 and 0.23 V are assigned to ligand-centered redox features and are similar to two of the four ligand-centered redox potentials for the Ni(^{H}NNNN^{H}) complex shown in Chart 2 (−0.41 and 0.02 V).[20] Using innocent NMe_2 substituents here in **1**, compared to redox-active NH_2 substituents in a similar system reported by Thomas et al., eliminates their additional ligand-centered redox waves at −1.75 and −1.04 V.[20]

The CV trace of **2** reveals similar ligand-centered redox events as **1** but differs in that the most negative redox couple assigned as Ni^{2+}/Ni^{1+} is irreversible for **2**. Scanning the full electrochemical window in THF reveals two irreversible one-electron reduction waves at E_{pc} −2.18 and −2.87 V along with additional features in the oxidation scan attributed to electrochemically active degradation products. Limiting the scans to only ±0.6 V vs Fc^+/Fc (Figure 2, right column) reveals two reversible one-electron exchange waves with $E_{1/2}$ values of −0.19 and 0.22 V assigned to ligand-centered redox events. The first ligand oxidation at −0.19 V is shifted 170 mV more positive compared to the same feature in the CV of **1** at −0.36 V, which reflects the decreased donor ability of the SMe groups in **2** vs the NMe_2 groups in **1**. In contrast, the second ligand oxidations at 0.23 and 0.22 V are nearly identical.

We previously reported two similar features in the CV trace of Ru(^{Me}SNNS^{Me})(PPh_3) in THF (where ^{Me}SNNS^{Me} = **L2**), albeit at more negative potentials (−0.78 and −0.28 V vs Fc^+/Fc).[31] An irreversible reduction wave was also observed at −2.46 V in the CV of Ru(^{Me}SNNS^{Me})(PPh_3) similar to that observed for **2**. Based on our analysis here, we can revise our tentative redox assignments made previously for the reversible one-electron waves at −0.78 and −0.28 V in Ru(^{Me}SNNS^{Me})(PPh_3)[31] as ligand-centered redox events assigned to **L2**.

We also collected the CV of **3** to evaluate the importance of the phenylene backbone in the redox chemistry of **1** and **2**. Scanning the full electrochemical window of **3** in THF yields a complicated CV with irreversible reduction waves at E_{pc} values of −2.72 and −2.04 V similar to those observed in the CV of **2** (Figure 2). Limiting the scanned electrochemical window as described above yields a cleaner CV trace with several quasi-reversible waves. The redox activity of the ligand in **3** is not eliminated completely by removing the phenylene backbone, although reversibility was clearly attenuated, as shown by lower peak current densities in the associated redox features. This suggests the isolated, flanking aryl groups still participate in ligand-centered redox reactions, even with innocent flanking donor substituents such as thioethers. Intuitively, it also provides compelling evidence that including the aromatic backbone between the two peripheral rings strengthens electrochemical communication of redox-active triaryl ligands in **1** and **2**.

Chemical Oxidations of 1 and 2. To investigate the chemical and electronic structures of the electrochemically generated species observed in the CV traces, **1** and **2** were chemically oxidized using silver salts. Similar studies were attempted with **3**, but we were unable to isolate pure compound from these mixtures. Singly oxidized complexes were generated by mixing one-to-one equivalents of **1** or **2** with $AgBF_4$ in CH_2Cl_2. After filtration to remove Ag(0), dark green crystals of **1**[BF_4] and **2**[BF_4] were obtained by layering the CH_2Cl_2 filtrate with Et_2O. ^1H and ^{13}C NMR spectra collected on dissolved crystalline material of **1**[BF_4] and **2**[BF_4] confirmed that the complexes were NMR silent, consistent with the formation of paramagnetic ligand-centered radicals. Only ^{11}B and ^{19}F resonances associated with the outer-sphere BF_4^- anions were observed. **1**[BF_4] revealed sharp resonances at δ −1.36 and −151.7 ppm in the ^{11}B and ^{19}F NMR spectra, respectively. **2**[BF_4] showed a similar resonance in the ^{11}B NMR spectrum at δ −1.12 ppm, but the ^{19}F NMR spectrum revealed an uncharacteristically shifted and broadened resonance at δ −149.4 ppm. The difference in ^{19}F

DOI: 10.1021/acs.inorgchem.9b01675
Inorg. Chem. 2019, 58, 12756−12774

NMR data for $1[BF_4]$ and $2[BF_4]$ suggests that outer-sphere BF_4^- anions interact more with the paramagnetic complex containing the thioether-substituted ligand **L2**. This observation was corroborated by EPR studies described in the following section (see below).

Attempts to oxidize $1[BF_4]$ and $2[BF_4]$ further using $AgBF_4$ were not productive because it afforded complex salts that were insoluble in all organic solvents we tested. Instead, the doubly oxidized complexes were prepared by treating CH_2Cl_2 solutions of **1** or **2** with 2 equiv of AgOTf or $AgNTf_2$. After filtration, dark purple blocks of $1[OTf]_2$ and $2[OTf]_2$ and green needles of $2[NTf_2]_2$ were grown by layering the CH_2Cl_2 filtrate with Et_2O. Unlike the NMR silent singly oxidized salts, several broad and paramagnetically shifted ^1H NMR resonances were observed at δ 2.40, 3.01, 12.73, 14.94, 21.13, and 39.44 ppm for $1[OTf]_2$. Broad ^1H resonances are also observed for $2[OTf]_2$ and $2[NTf_2]_2$.

^{19}F NMR spectroscopy was again used to confirm the presence of the fluorinated outer-sphere anions. The ^{19}F NMR spectrum of $1[OTf]_2$ revealed a broad peak at δ −38.5 ppm that was shifted significantly from where free triflate is typically observed in diamagnetic salts (δ −74 to −77 ppm).[41] Similarly, a broad ^{19}F resonance is observed for $2[OTf]_2$ at δ −41.7 ppm. Like the NMR studies of singly oxidized $2[BF_4]$, the change in ^{19}F NMR shifts for $1[OTf]_2$ and $2[OTf]_2$ suggested that the triflate anions are bound in solution, as observed in solid-state XRD studies (see below). In contrast, the ^{19}F NMR spectrum of $2[NTf_2]_2$ revealed only a slight shift in the ^{19}F resonance at δ −72.2 ppm compared to that typically reported for free triflimidate at δ −76.0 ppm,[42,43] consistent with the decreased coordination ability of triflimidate relative to triflate.

UV−vis-NIR Spectroscopy. UV−vis data were collected for **1**−**3** to analyze their electronic structure differences as a function of ligand modifications and counteranions (Figure 3).

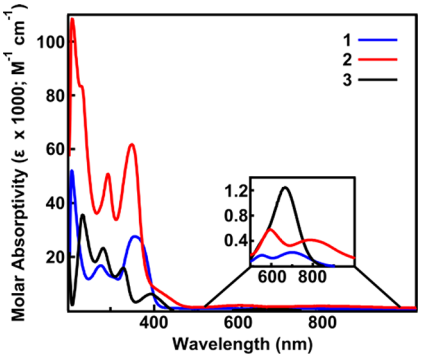

Figure 3. Comparison of UV−vis spectra for neutral complexes **1**, **2**, and **3**. The inset shows the magnified visible region with the dipole forbidden d−d transitions. Data were collected on 50 μM (UV) and 800−1200 μM (vis) solutions in DCM at 298 K.

The UV−vis spectrum of **1** shows three intense charge transfer bands at 210, 278, and 355 nm that are assigned to either ligand−ligand charge transfer (LLCT) or metal−ligand charge transfer (MLCT) transitions. Complex **2** also shows three similar UV−vis absorption features at similar energies of 215, 296, and 350 nm, albeit with increased intensity relative to those in **1**. The spectrum of **2** contains an additional shoulder at 230 nm that was not observed in the spectrum of **1**. Two weak absorptions assigned to dipole-forbidden d−d transitions were observed at 558 and 704 nm for **1**, and these shift to lower energies in the spectrum of **2** (598 and 800 nm, respectively).

The UV−vis spectrum of **3** helped to elucidate the origin of some of the spectral features for **1** and **2**. The highest-energy absorption band of **1** and **2** (210 and 215 nm, respectively) is absent in the spectrum of **3**, suggesting that this feature is associated with the *o*-phenylenediamine subunit. The highest energy absorption feature for **3** is significantly lower at 240 nm, which appears to correspond with the additional shoulder observed in the UV−vis spectrum of **2** at ca. 230 nm. The absence of this shoulder in the spectrum of **1** suggests that these absorptions are associated with LLCT transitions involving the SMe groups on **2** and **3**. The other notable difference in the spectra of **3** is the more intense d−d transition at 671 nm which displays a slight high-energy shoulder (Figure 3). This suggests that the two d−d transitions observed in the spectra of **1** and **2** are less resolved in the spectrum of **3**.

We next compared the change in the UV−vis-NIR spectra of **1** and **2** as they were chemically oxidized (Figure 4). Oxidation

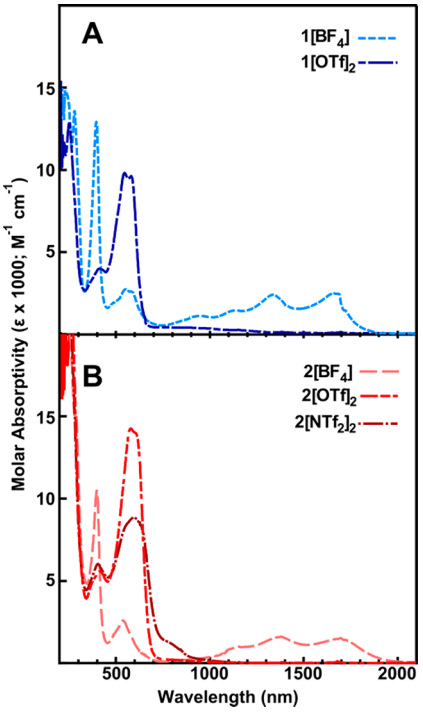

Figure 4. UV−vis-NIR data collected for the singly and doubly oxidized complexes. (A) Comparison of $1[BF_4]$ and $1[OTf_2]_2$. (B) Comparison of $2[BF_4]$, $2[OTf]_2$, and $2[NTf_2]_2$. Data were collected on 50 μM (UV) and 250 μM (vis-NIR) solutions in DCM at 298 K.

of **1** attenuates the most intense charge transfer transitions in the spectra of $1[BF_4]$ and $1[OTf]_2$, and similar observations are made for oxidation of **2**. A prominent absorption observed at 395 nm for $1[BF_4]$ and $2[BF_4]$ decreases in intensity for the doubly oxidized complexes. The dipole-forbidden d−d transitions increase in intensity but are located at similar energies as those observed for neutral **1** and **2**. The NIR region of singly oxidized complexes revealed the appearance of new low-energy peaks at 1124, 1336, and 1674 nm for $1[BF_4]$ and 1155, 1373, and 1690 for $2[BF_4]$. These are commonly assigned as intervalence charge transfer (IVCT) bands and are indicative of a delocalized ligand-centered radical (Figure 4).[44]

DOI: 10.1021/acs.inorgchem.9b01675
Inorg. Chem. 2019, 58, 12756−12774

As expected, the IVCT bands do not appear in the NIR spectra of the doubly oxidized complexes.

Structural Analysis of the Oxidized Complexes. XRD data were collected on single crystals of the oxidized complexes so their bond distances and structures could be compared as a function of oxidation state. Singly oxidized **1**[BF_4] and **2**[BF_4] revealed monomeric structures with outer-sphere BF_4^- anions. Notably, the structure of the thioether-substituted congener **2**[BF_4] features two Ni complexes that were stacked close together (Figure 5). The intermetallic Ni···Ni distance of

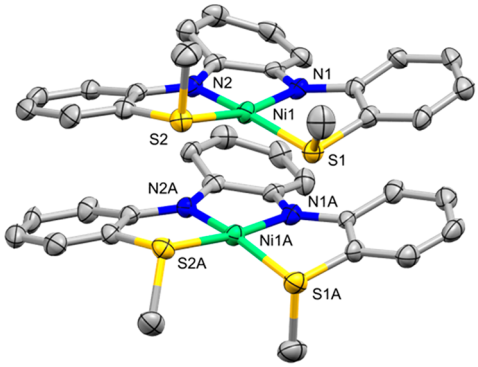

Figure 5. Molecular structure of **2**[BF_4] from single-crystal XRD studies. Ellipsoids are drawn at the 50% probability level. Hydrogen atoms and outer-sphere BF_4^- were omitted from the figure.

3.264(1) Å is longer than the Ni−Ni distance in a structurally similar $[Ni(^{H}NNNN^{H})]_2^{2+}$ dimer reported by Thomas and co-workers (2.784 Å).[20] The close Ni···Ni distance in **2**[BF_4] relative to monomeric **1**[BF_4] is attributed to the additional conformational flexibility of the methyl substituents attached to sulfur in **L2**, which can rotate away from one face of the Ni complex to accommodate stacking between the two units. In contrast, the methyl substituents on the more rigid NMe_2 groups in **1**[BF_4] project axially on both sides of the square plane and block similar $\pi-\pi$ stacking.

XRD data collected for the doubly oxidized complexes **1**[OTf]$_2$ and **2**[OTf]$_2$ revealed octahedral coordination geometries with *trans* triflate anions bound to Ni (Figure 6). The Ni−O distances were 2.160(2) and 2.145(2) Å in **1**[OTf]$_2$ and 2.147(2) and 2.069(2) Å in **2**[OTf]$_2$. These structures confirm the ^{19}F NMR results that showed larger than expected chemical shifts based on comparison to free triflate. In contrast, the structure of **2**[NTf_2]$_2$ showed no significant interaction with the outer-sphere triflimidate anions, again consistent with the ^{19}F NMR data. The closest triflimidate atom to nickel was an oxygen with a Ni−O distance of 2.794(2) Å.

The average Ni−N bond distances associated with the *o*-phenylenediamine backbone are similar in **1** and **1**[BF_4] at 1.837 and 1.849 Å, respectively, but increase to 1.997 Å as the coordination number changes from four to six (Table 1). A nearly identical trend with similar values was observed for **2**, **2**[BF_4], and **2**[OTf]$_2$. Comparison of the average Ni−N distances in six-coordinate **2**[OTf]$_2$ at 2.003 Å to those in four-coordinate **2**[NTf_2]$_2$ at 1.872 Å indicates that larger changes in bond distance are primarily due to changes in coordination number. This is further supported by comparison of the average Ni−S distances: only a small stepwise increase is observed for **2** (2.153 Å), **2**[BF_4] (2.161 Å), and **2**[NTf_2]$_2$ (2.191 Å), but this increases more abruptly to 2.385(1) Å in six-coordinate **2**[OTf]$_2$.

We next analyzed how oxidation and ligand substituents affect the four-coordinate geometry around Ni (Table 3). All

Table 3. Deviations from Square Planar to Tetrahedral Geometry for Four-Coordinate Complexes

	θ (deg)	$\tau_{sq\text{-}tet}$ (θ/90°)
tetrahedral	90	1
sq. planar	0	0
1	6.6	0.07
1[BF_4]	3.1	0.03
2	12.1	0.13
2[BF_4]	13.4	0.15
2[NTf_2]$_2$	3.9	0.04

of the four-coordinate complexes are roughly square planar, and we used the angle θ between the two planes defined by N−Ni−N and S−Ni−S to quantify the distortion toward

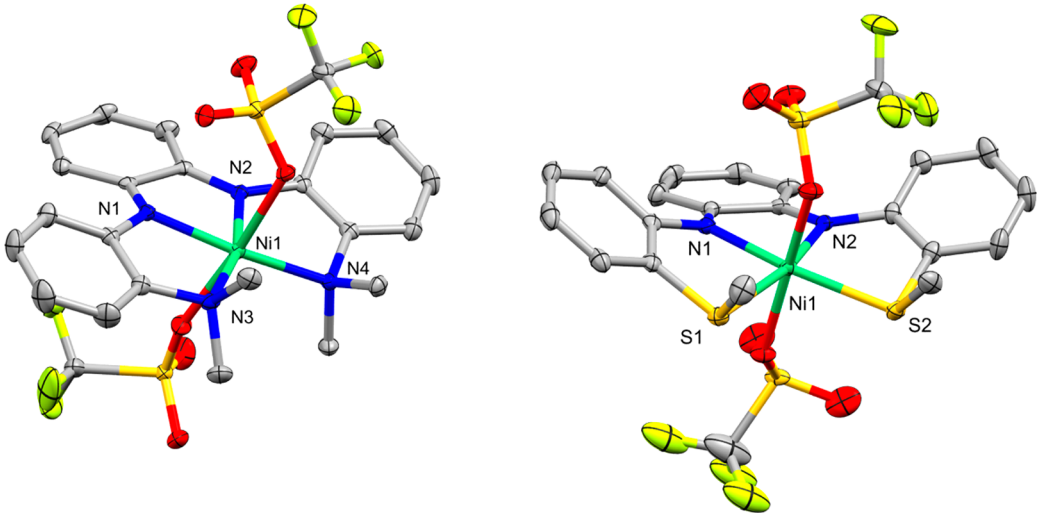

Figure 6. Molecular structures of **1**[OTf]$_2$ (left) and **2**[OTf]$_2$ (right) from single-crystal XRD studies. Ellipsoids are drawn at the 50% probability level. Hydrogen atoms were omitted from the figure.

DOI: 10.1021/acs.inorgchem.9b01675
Inorg. Chem. 2019, 58, 12756−12774

tetrahedral (Figure 7). As shown in Table 3, the neutral and singly oxidized complexes with **L2** (X = SMe) show greater

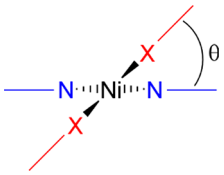

Figure 7. Angle used to quantify deviation from square planar geometry.[45]

deviations from planarity relative to those in **L1** (X = NMe_2) presumably due to the more weakly coordinating and asymmetric thioether groups. Single oxidation of **1** and **2** had only a subtle change on the degree of distortion in the structure of **1**[BF_4] and **2**[BF_4], but the structure of doubly oxidized **2**[NTf_2]$_2$ showed a significant decrease in θ consistent with increased sp^2 character on N in the *o*-phenylenediamine backbone due to multiple ligand-centered oxidations.

The change in ligand bond distances for **1** and **2** matches those expected for stepwise oxidation of *o*-phenylenediamine (as shown in Chart 1) and contrasts the changes reported previously for Ni(^{H}NNNN^{H}) complexes with redox-active flanking NH substituents. The dominant resonance structures for **1**, **1**$^{+}$, and **1**$^{2+}$ are shown in Figure 8 based on the observed changes in bond distances from the single-crystal XRD data. Upon oxidation, the average N−C bond distances associated with the *o*-phenylenediamine subunit decrease from 1.392(8) (**1**) to 1.357(6) (**1**[BF_4]) to 1.308(4) Å (**1**[OTf]$_2$) corresponding to an increase in double bond character (Figure 8a). A complementary increase is observed in the backbone NC−CN bond distance from 1.433(6) to 1.449(4) to 1.512(4) Å corresponding to an increase in single bond character (Figure 8a). Similar trends are observed in the stepwise oxidation of **2** (Table 1). For comparison, the neutral Ni(^{H}NNNN^{H}) diradical complexes depicted in Figure 8b undergo stepwise ligand-centered oxidations on the peripheral aryl groups.

In general, bond distances for the doubly oxidized complexes **1**$^{2+}$ and **2**$^{2+}$ suggest formation of the *o*-diiminoquinone, as shown in Figure 8a. However, one of the more interesting structural comparisons concerns the ligand bond distances in four-coordinate **2**[NTf_2]$_2$ and six-coordinate **2**[OTf]$_2$. As shown in Table 1, the NC−CN bond distances are slightly shorter in **2**[NTf_2]$_2$ at 1.484(3) Å compared to 1.505(5) Å in **2**[OTf]$_2$. Likewise, all of the N−C bond distances are slightly longer in the structure of **2**[NTf_2]$_2$. As we will show, these subtle differences in ligand bond distances foreshadow more pronounced differences in the electronic structure of **2**$^{2+}$ when anions bind to Ni.

Magnetic Susceptibility Measurements. To determine the number of unpaired electrons present in the oxidized complexes, their magnetic susceptibilities were determined using the Evans method.[46,47] The results are compiled in Table 4 alongside the theoretical spin-only values expected for

Table 4. Average Evans Method Magnetic Susceptibility Values for Singly and Doubly Oxidized Complexes of 1 and 2 Reported in Units of Bohr Magnetons (μ_B) from Triplicate Measurements[a]

singly oxidized		doubly oxidized	
1[BF_4]	1.6(1)	**1**[OTf]$_2$	2.9(2)
1[NTf_2]	1.6(1)		
2[BF_4]	1.7(1)	**2**[OTf]$_2$	2.5(2)
2[NTf_2]	1.5(2)	**2**[NTf_2]$_2$	1.9(1)
theoretical (S = 1/2)	1.73	theoretical (S = 1)	2.83

[a]Theoretical spin-only values are included for comparison. Measurements were collected in DCM at 298 K with a protio/deuterated DCM capillary insert and in a range of 2−10 μM.

doublet (S = 1/2) and triplet (S = 1) electron configurations. The singly oxidized complexes are all close to the spin-only value of 1.73 μ_B, as would be expected for the *o*-diiminosemiquinone. However, the doubly oxidized complexes show a greater range of magnetic susceptibilities. The triflate complexes **1**[OTf]$_2$ and **2**[OTf]$_2$ are both close to the spin-only value for an S = 1 configuration at 2.9(2) and 2.5(2) μ_B (theoretical 2.83 μ_B), but the triflimidate complex **2**[NTf_2]$_2$ was significantly lower at 1.9(1) μ_B, which is closer to the S = 1/2 value. Variable temperature Evans method experiments with **2**[NTf_2]$_2$ revealed Curie−Weiss behavior between the temperatures of −80 and 30 °C where the μ_{eff} spin value increases to a maximum of 2.15 μ_B at the lowest temperature (−80 °C). Plotting χ_M^{-1} against temperature shows that **2**[NTf_2]$_2$ displays antiferromagnetic behavior (Weiss constant: θ < 0) (Figure S51).[48]

EPR Spectroscopy. EPR data were collected to investigate the distribution of unpaired electron spins in all of the oxidized

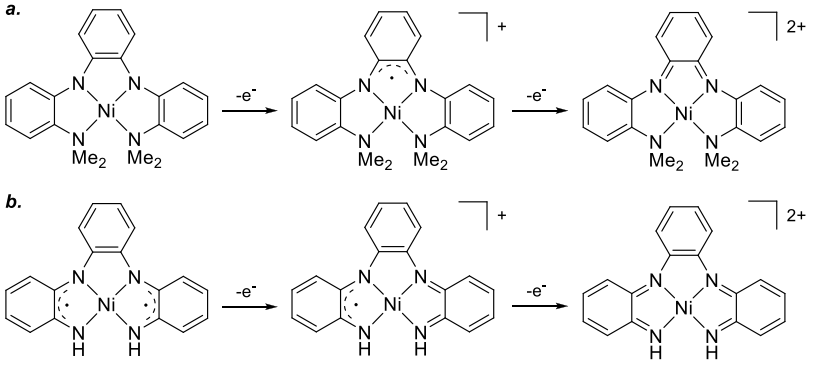

Figure 8. Comparison of dominant Lewis structures based on single-crystal XRD data for sequential oxidation of (a) **1** with flanking NMe_2 substituents and (b) Ni(^{H}NNNN^{H}) complexes with flanking NH substituents from ref 19. The *tert*-butyl substituents attached to the flanking aryl groups (as shown in Chart 2) were omitted from the figure in part b.

DOI: 10.1021/acs.inorgchem.9b01675
Inorg. Chem. 2019, 58, 12756−12774

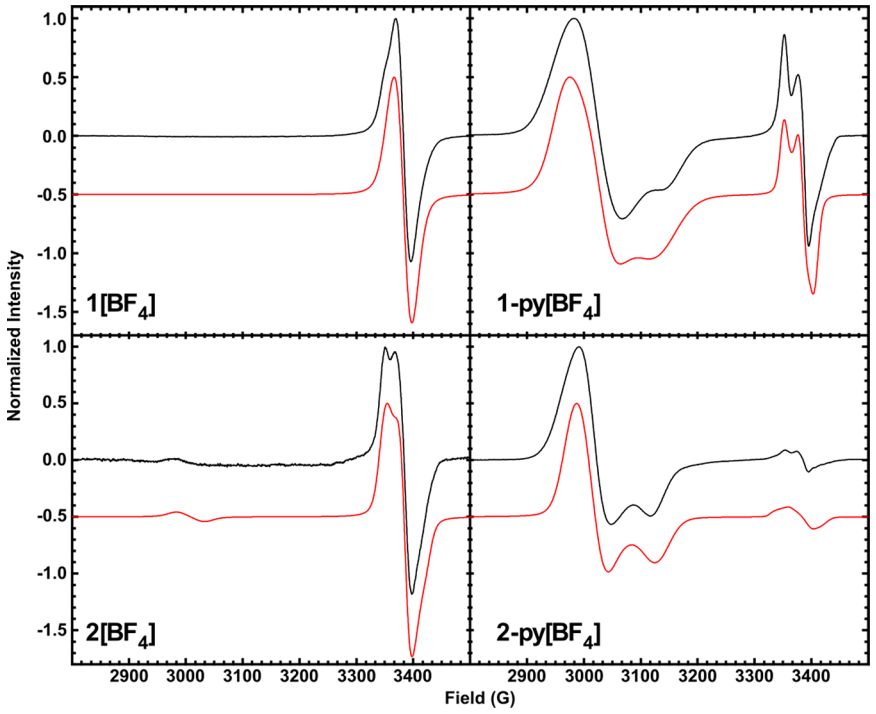

Figure 9. (left) X-band EPR spectra of native $\mathbf{1}[\mathbf{BF_4}]$ and $\mathbf{2}[\mathbf{BF_4}]$ at 109 K. (right) X-band EPR spectra of $\mathbf{1}[\mathbf{BF_4}]$ and $\mathbf{2}[\mathbf{BF_4}]$ at 109 K in the presence of excess pyridine. Experimental spectra were collected in neat DCM. Simulated data are shown in red.

complexes. Initial experiments were performed by dissolving crystalline material into neat DCM. The room-temperature spectra of singly oxidized $\mathbf{1}[\mathbf{BF_4}]$ and $\mathbf{2}[\mathbf{BF_4}]$ revealed an isotropic signal at g_{iso} = 2.008 consistent with the presence of a ligand-centered radical. However, upon cooling to 109 K, subtle differences between the two compounds were observed. The low-temperature (LT) EPR data of $\mathbf{1}[\mathbf{BF_4}]$ show a slightly distorted isotropic signal with g_{iso} = 2.007. The LT-EPR data of $\mathbf{2}[\mathbf{BF_4}]$ revealed a similar axial signal at $g \sim 2$ but also a low-intensity spectroscopic feature around $g \sim 2.2$ (Figure 9). The signals around $g \sim 2$ are typical of the $S = 1/2$ ground state for systems containing an *o*-iminosemiquinone radical, whereas the signal at $g \sim 2.2$ is commonly assigned to Ni(III).[49−52] No hyperfine splitting is observed with the *o*-phenylenediamine nitrogen atoms, similar to that reported for square planar Ni(III) salophen complexes.[52]

Previous reports of closely related nickel complexes with tetradentate Schiff-base ligands describe how a ligand-derived singly occupied molecular orbital (SOMO) can transition to a metal-based SOMO via valence tautomerization.[53,54] This type of tautomerization can be further defined as *temperature-dependent* (where population of the SOMO changes as a function of temperature, thereby resulting in relative changes in different signal intensities) or as *coordination-induced* (where coordination to the metal destabilizes a metal-based orbital to yield a new spectroscopic signal).[54−56]

To investigate possible temperature dependent tautomerism, variable-temperature EPR spectroscopic experiments of $\mathbf{2}[\mathbf{BF_4}]$ were conducted in 2-MeTHF/DCM (1:3) solutions. Upon cooling to 109 K, the Ni(III) signals at g_{iso} = 2.215 became more well resolved and showed satellite peaks to either side of the isotropic signal (Figure 10). However, warming the sample and collecting spectra showed that metal and organic signal intensities decrease uniformly (Figure S35), ruling out temperature-dependent valence tautomerism. This suggested

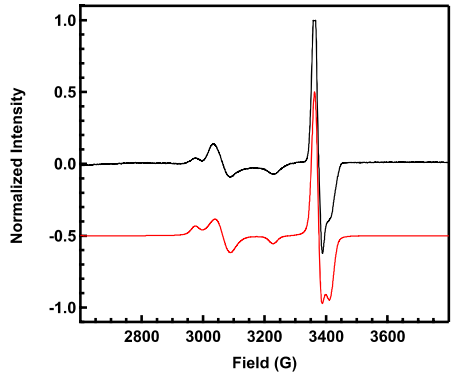

Figure 10. EPR spectrum of $\mathbf{2}[\mathbf{BF_4}]$ at 109 K experimental spectra (black) and simulated spectra (red). Spectrum collected in 2-MeTHF/DCM (1:3).

that the new spectroscopic EPR feature was coordination-induced, presumably due to interactions between the nickel center in $\mathbf{2}[\mathbf{BF_4}]$ and the BF_4^- anion. Evidence of this Ni···F−BF_3 interaction in the EPR spectrum of $\mathbf{2}[\mathbf{BF_4}]$ and not $\mathbf{1}[\mathbf{BF_4}]$ is consistent with the decreased steric profile of SMe vs NMe_2 and the increased Lewis acidity of Ni in $\mathbf{2}[\mathbf{BF_4}]$. As described in the comparison to the XRD data, the fluxional SMe substituents in $\mathbf{2}[\mathbf{BF_4}]$ can rotate away from one axial face to allow the BF_4^- anion to interact with Ni in solution. Indeed, simulations required modeling a ^{19}F hyperfine splitting interaction (A = 777 MHz) at g = 2.186 and an isotropic Ni(III) feature at g_{iso} = 2.215, indicating an interaction between the counteranion and the complex cation (Figure 10). The magnitude of the hyperfine splitting with axial ^{19}F is consistent with EPR data reported for other Ni(III) complexes with Ni−F bonds.[57]

To further test our hypothesis regarding the coordination-induced valence tautomerism, we performed two experiments:

DOI: 10.1021/acs.inorgchem.9b01675
Inorg. Chem. 2019, 58, 12756−12774

Table 5. Calculated g Values from Simulated EPR Spectra of Singly Oxidized Complexes Collected in DCM at 109 K

	Ni(III) region				ligand radical region			
compound	g_{xx}	g_{yy}	g_{zz}	g_{iso}[b]	g_{xx}	g_{yy}	g_{zz}	g_{iso}[b]
1[BF_4]								2.007
1-py[BF_4][c]	2.287	2.240	2.167	2.231	2.025	2.005	1.993	2.007
1[NTf_2]								2.007
1-py[NTf_2][c]	2.275	2.213	2.164	2.217	2.025	2.005	1.992	2.007
2[BF_4][d]	2.224		2.206	2.215	2.016	2.008	1.985	2.003[a]
2[BF_4]				2.256	2.025	2.003	1.992	2.007
2-py[BF_4][c]	2.263	2. 261	2.170	2.231	2.029	2.006	1.990	2.008
2[NTf_2]								2.010
2-py[NTf_2][c]	2.266	2.222	2.184	2.205	2.024	2.012	2.004	2.008[a]

[a]Values determined at RT. [b]Calculated average values. [c]Experiments were conducted in the presence of 3000 equiv of pyridine. [d]Collected in 2-MeTHF/DCM. [e]Fluorine splitting was modeled as a separate $S = 1/2$ species with $g_{iso} = 2.186$ and $A = 11.62$, 8.45, and 777.41 MHz.

(1) We replaced the BF_4^- anion with more noncoordinating triflimidate (NTf_2^-), and (2) we recollected the EPR data on **1**[BF_4] and **2**[BF_4] in the presence of excess pyridine, as has been described for other singly oxidized Ni complexes with redox-active ligands.[52,58−62] The singly oxidized triflimidate complexes **1**[NTf_2] and **2**[NTf_2] were prepared as described for the BF_4 salts by treating **1** and **2** with 1 equiv of $AgNTf_2$ in DCM. Filtering the reaction mixture and layering with Et_2O afforded dark green crystals of **1**[NTf_2] and **2**[NTf_2]. Similar to **1**[BF_4] and **2**[BF_4], the triflimidate salts were ^1H NMR silent but produced sharp and unshifted ^{19}F signals (δ −79.2 and −78.8 ppm, respectively),[42] suggesting little to no interaction with the native oxidized complexes. Subsequent EPR investigations led to only isotropic resonances centered at $g \sim 2$ at both RT and 109 K for **1**[NTf_2] and **2**[NTf_2] (Figures S38 and 39 and S43 and S44, respectively). No Ni(III) signals were observed, thereby confirming the lack of significant interactions between the complex cations and the non-coordinating triflimidate anions in solution.

Next, excess dry pyridine was added to neat DCM solutions of **1**[BF_4], **1**[NTf_2], **2**[BF_4], and **2**[NTf_2] and their EPR spectra were collected. At room temperature, the EPR spectrum for **2**[BF_4] with excess pyridine yielded a resolved isotropic signal at $g \sim 2.20$, suggesting pyridine coordination to the Ni (Figure S42). In contrast, the room-temperature EPR spectrum for **1**[BF_4] with pyridine still shows only an isotropic resonance at $g \sim 2$ (Figure S37). However, decreasing the temperature to 109 K revealed the appearance of a strong signal at $g_{iso} = 2.231$ for **1**[BF_4]. A smaller isotropic signal is observed in both low-temperature spectra with pyridine, but the resonance at $g \sim 2.22$ for **2**[BF_4] is more intense relative to the smaller isotropic resonance observed for **1**[BF_4] (Figure 9). Results for **1**[NTf_2] and **2**[NTf_2] mimic the results for **1**[BF_4] and **2**[BF_4] (Figures S38−S41 and S43−S46). Overall, the differences in pyridine binding are again consistent with the decreased steric profile of SMe and the increased Lewis acidity of Ni in $\mathbf{2}^+$, as has been described in pyridine binding studies with different singly oxidized Ni complexes with redox-active salen ligands.[61] Furthermore, the Ni(III) EPR resonances for the pyridine coordinated spectra indicate $g_\perp > g_\parallel$, suggesting that coordination involves the axial d_z^2 orbital on Ni (Table 5). In general, this is well precedented for square planar complexes,[52,49,63] although exceptions do exist.[64]

The EPR results suggest that the singly oxidized complexes undergo coordination-induced valence tautomerism according to the following expression (eq 1):[61]

$$[Ni^{II}(L^{\bullet})]^+ + n(py) \rightleftharpoons [Ni^{III}(L)](py)_n \quad (1)$$

The final question for the results with pyridine concerns the number or pyridine ligands that bind to Ni (n in eq 1). It is known that pyridine addition to singly oxidized Ni complexes containing redox-active ligands typically yields octahedral complexes with two pyridines bound to the metal,[52,58−62] although examples of five-coordinate complexes with one bound pyridine are also known.[62] Addition of pyridine to solutions of **2**[BF_4] and **2**[NTf_2] resulted in an immediate color change, but we were unable to isolate and structurally characterize the resulting products to determine the number of metal-bound pyridine ligands. However, UV−vis titration studies of **2**[NTf_2] with excess pyridine suggested that only one pyridine binds to nickel (Figure 11). While we cannot

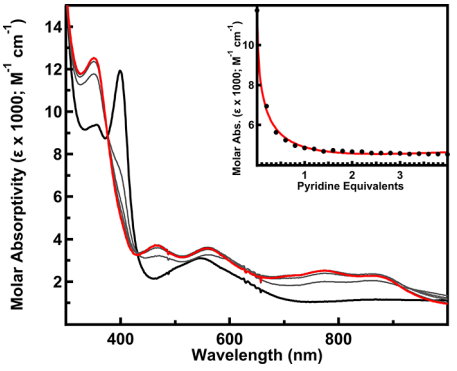

Figure 11. UV−vis pyridine titration studies of **2**[NTf_2] in THF at 298 K. Inset: change in the molar absorptivity of the peak at 399 nm. The solid line represents the nonlinear least-squares fit for 1:1 complex formation.

completely rule out that more than one pyridine binds to the metal at lower temperatures, especially in the presence of a large excess of pyridine, DFT calculations corroborate our UV−vis titration and suggest that only one pyridine binds. Notably, attempts to optimize structures of $\mathbf{2}^+$ with two pyridine ligands bound to Ni resulted in one of the pyridine ligands being expelled out of the coordination sphere to form a five-coordinate square pyramidal Ni complex with Ni−pyridine distances of 2.183 and 4.553 Å (Figure S55).

Motivated by the paramagnetically shifted ^1H NMR spectra and magnetic susceptibility results for doubly oxidized **1**[OTf]$_2$, **2**[OTf]$_2$, and **2**[NTf_2]$_2$ (Table 4), EPR spectroscopic data were collected on these compounds to determine if

DOI: 10.1021/acs.inorgchem.9b01675
Inorg. Chem. 2019, 58, 12756−12774

EPR signals associated with their unpaired spins could be observed. In this context, we note that high-spin $S = 1$ Ni complexes with metal-centered spin density often have signals that are too broad to be observed without a high-field EPR (HFEPR) spectrometer.[65−67] However, room-temperature EPR data collected in 2-MeTHF/DCM (1:3) showed isotropic signals centered at $g \sim 2$. Subsequent low-temperature data collected at 109 K revealed broad features at $g_{iso} = 2.016$, 2.014, and 2.013 for $\mathbf{1}[\mathbf{OTf}]_2$, $\mathbf{2}[\mathbf{OTf}]_2$, and $\mathbf{2}[\mathbf{NTf_2}]_2$, respectively, with some hyperfine structure (Figure 12 and Figure S49). Additionally, no half-field triplet signal implicating an organic diradical was observed in the $g = 4$ region. Simulations and least-squares fits of the low-temperature EPR data corroborated the high-spin configuration and required modeling with small zero-field splitting parameters of $D = 2.9 \times 10^{-4}$, 7.3×10^{-4}, and 7.2×10^{-4} cm^{-1} and $E = 1.8 \times 10^{-4}$, 9.9×10^{-5}, and 8.9×10^{-5} cm^{-1} for $\mathbf{1}[\mathbf{OTf}]_2$, $\mathbf{2}[\mathbf{OTf}]_2$, and $\mathbf{2}[\mathbf{NTf_2}]_2$, respectively.

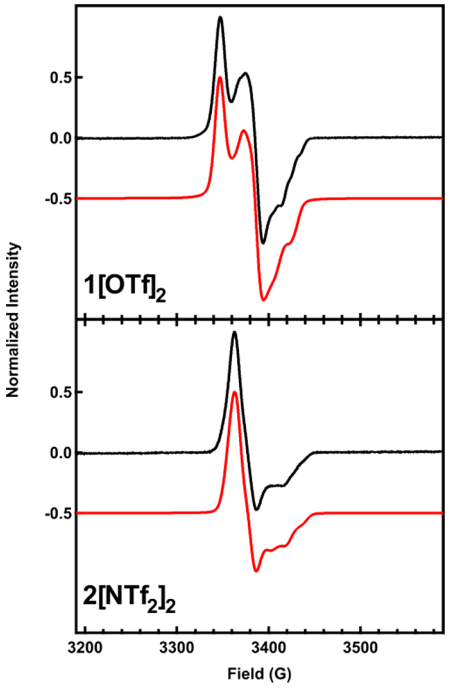

Figure 12. EPR spectra of $\mathbf{1}[\mathbf{OTf}]_2$ and $\mathbf{2}[\mathbf{NTf_2}]_2$ in 2-MeTHF/DCM (1:3) at 109 K (g_{iso}= 2.016 and 2.013, respectively). Experimental data (black) and simulated trace (red).

Collectively, these results closely match EPR data reported previously for bimetallic biradical complexes containing two redox-active ligand centers separated by a structural linker.[68,69] It has been shown that the linkers in these systems serve to isolate and spatially localize the two radicals on the two different metallic fragments, thereby leading to very weak electron coupling and remarkably small zero-field splitting on the order of 10^{-4} cm^{-1}.[68,69] By way of comparison, it remains unclear as to why the radicals would be so localized in our complex to give similar EPR spectra, especially when considering the significant differences in calculated spin density, electronic structure, and corroborating X-ray absorption spectroscopy results described in the following sections. Additional experiments to account for these EPR data are ongoing.

Density Functional Theory Calculations. DFT calculations were used to evaluate the electronic structure and spin density variations of **1** and **2** upon stepwise oxidation and in the presence of axially coordinating ligands. All gas-phase geometry optimizations were performed using B3LYP/6-31G(d,p). The calculated bond distances and angles are in relatively good agreement with the experimental structures and follow the same general trends (Table S5). For example, the calculated Ni−N distances in the optimized structure of $\mathbf{1}[\mathbf{BF_4}]$ of 1.837 and 1.838 Å are very close to the experimental values of 1.853(3) and 1.845(3) Å (Table 1). Likewise, the calculated Ni−N bond distances in doubly oxidized $\mathbf{1}[\mathbf{OTf}]_2$ increase to 1.999 and 2.008 Å, as observed in the experimental structure (1.992(2) and 2.002(3) Å; Table 1).

Calculations on the doubly oxidized complexes suggest that the triplet ground states ($S = 1$) are lower in energy compared to the singlet ground states ($S = 0$), corroborating experimental observations of unpaired spin in the doubly oxidized complexes. The triplet states calculated for $\mathbf{1}[\mathbf{OTf}]_2$ and $\mathbf{2}[\mathbf{OTf}]_2$, for example, were 18 and 23 kcal/mol lower in energy than their respective closed-shell singlet states. Furthermore, we saw no evidence suggesting a more stable open-shell singlet state for $\mathbf{1}[\mathbf{OTf}]_2$ and $\mathbf{2}[\mathbf{OTf}]_2$, as indicated by minimal spin contamination of the singlet and S^2 being close to zero.[70] However, in the case of $\mathbf{2}[\mathbf{NTf_2}]_2$, the energy of the triplet is calculated to be within DFT error of the higher energy open-shell singlet (0.6 kcal/mol). For reference, the error in calculated singlet−triplet gaps using conventional DFT is typically around 2−3 kcal/mol.[71,72] The thermally accessible singlet state for $\mathbf{2}[\mathbf{NTf_2}]_2$ may account for its decreased solution magnetic moment compared to $\mathbf{1}[\mathbf{OTf}]_2$ and $\mathbf{2}[\mathbf{OTf}]_2$ (Table 4) and observed temperature dependence (i.e., increasing spin value with decreasing temperature).

The calculations for the singly oxidized complexes $\mathbf{1}[\mathbf{BF_4}]$ and $\mathbf{2}[\mathbf{BF_4}]$ revealed that the $S = 1/2$ spin density is primarily ligand-centered and delocalized over the π-conjugated triaryl framework (Figure 13). In order to determine if the metal···F−BF_3^- interactions had any effect on spin density, especially with the more exposed axial coordination site in $\mathbf{2}^+$, calculations were performed with BF_4^- located at different positions around the metal complexes. Indeed, a small amount of spin density was delocalized from Ni onto one of the fluorine atoms on BF_4^- when positioned close to Ni (Figure S54), but no obvious change in spin density was observed on the **L2** ligand. A similar result was observed in calculations on a hypothetical structure of $\mathbf{2}$-$\mathbf{py}[\mathbf{BF_4}]$ with pyridine bound to Ni in the axial position; a small amount of spin density was transferred from Ni to the nitrogen on pyridine, but there was no obvious change in calculated spin density on the conjugated **L2** backbone (Figure 13). Together, these results corroborate the additional structure in the low-temperature EPR spectrum of $\mathbf{2}[\mathbf{BF_4}]$ in 2-MeTHF/DCM (Figure 10). The minimum observed at 3125 G in the EPR spectrum of $\mathbf{2}$-$\mathbf{py}[\mathbf{BF_4}]$ splits into two peaks in the spectrum of $\mathbf{2}[\mathbf{BF_4}]$, consistent with hyperfine splitting due to coupling with one ^{19}F nucleus on BF_4^-.

We next performed the same spin density calculations for the doubly oxidized $\mathbf{1}^{2+}$ and $\mathbf{2}^{2+}$ with both triflate and triflimidate counteranions. Interestingly, the optimized DFT structure of $\mathbf{2}[\mathbf{NTf_2}]_2$ resulted in the triflimidate counterion binding to Ni in contrast to the experimental XRD structure that shows no such binding. The Ni−O distances decreased from 2.794(2) and 2.847(3) Å in the XRD structure of

DOI: 10.1021/acs.inorgchem.9b01675
Inorg. Chem. 2019, 58, 12756−12774

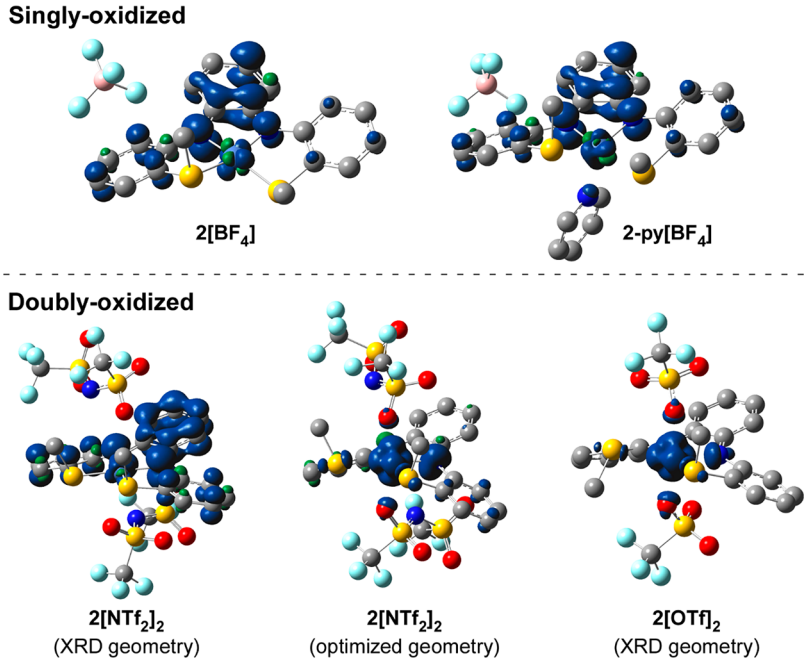

Figure 13. Spin density plots for singly and doubly oxidized complexes of **2**. Spin density isovalues are shown at 0.004 for comparison between each species. Hydrogen atoms on each complex were omitted from the figure.

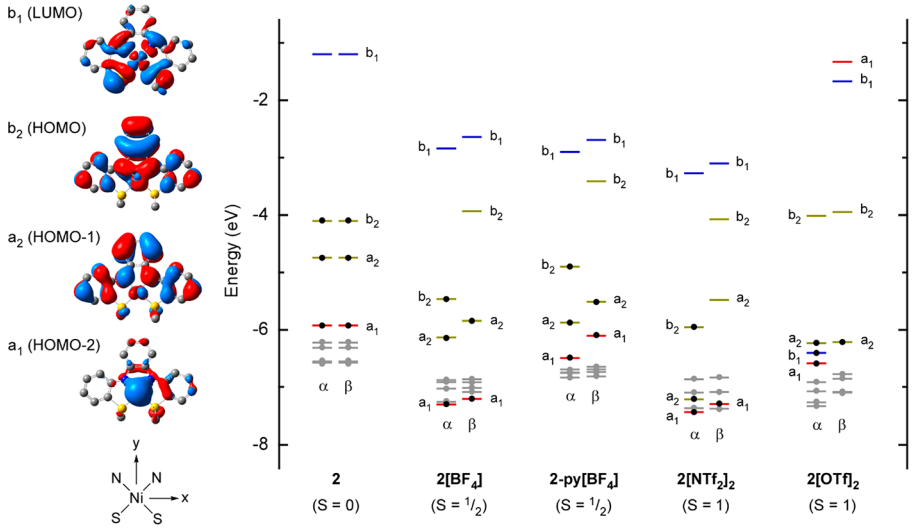

Figure 14. MO correlation diagram for neutral and oxidized complexes of **2** with different ancillary ligands and anions. Data shown for the oxidized complexes are from DFT-optimized structures with the exception of **2**[NTf_2]$_2$, which are from a calculated structure constrained to match the XRD coordinates to prevent NTf_2^- coordination to Ni. Select Kohn−Sham orbitals calculated for **2** are shown on the left and color-coded in the diagram to show how they transform across the series (metal-based b_1 = blue, a_1 = red; ligand-based b_2 and a_2 = gold). Mulliken symbol assignments were made by assuming C_{2v} point group symmetry and using the coordinate system shown. The principal C_2-axis used to assign the Mulliken symbols is labeled as *y*.

2[NTf_2]$_2$ to 2.171 and 2.223 Å in the optimized DFT structure (Table S5). To compare the spin density differences between the two structures, a DFT calculation was performed on **2**[NTf_2]$_2$ with the structure constrained to match the experimentally derived coordinates from the XRD data (Figure 13). Overall, the DFT calculations revealed significant differences in spin density that depend on coordination of the counteranion to Ni. In the absence of axial coordination with triflimidate in **1**[NTf_2]$_2$ and **2**[NTf_2]$_2$ (as observed in the experimental solid-state structures), the excess spin density localizes almost exclusively on the ligand (Figure 13). However, in stark contrast, triflate coordination to Ni in **1**[OTf]$_2$ and **2**[OTf]$_2$ causes the ligand-centered spin density to localize on the metal and metal-bound ligand atoms. Likewise, spin density calculations on the optimized gas-phase structure of **2**[NTf_2]$_2$ with bound triflimidate also show spin localization on the metal, albeit to a lesser extent than that observed for **2**[OTf]$_2$. A similar calculation on **2**[OTf]$_2$ with the structure constrained to match the coordinates obtained from XRD studies was performed, but no remarkable differences were observed when compared to the optimized structure (Figure 13). Overall, the qualitative differences in calculated OTf^- and NTf_2^- metal binding are consistent with

DOI: 10.1021/acs.inorgchem.9b01675
Inorg. Chem. 2019, 58, 12756−12774

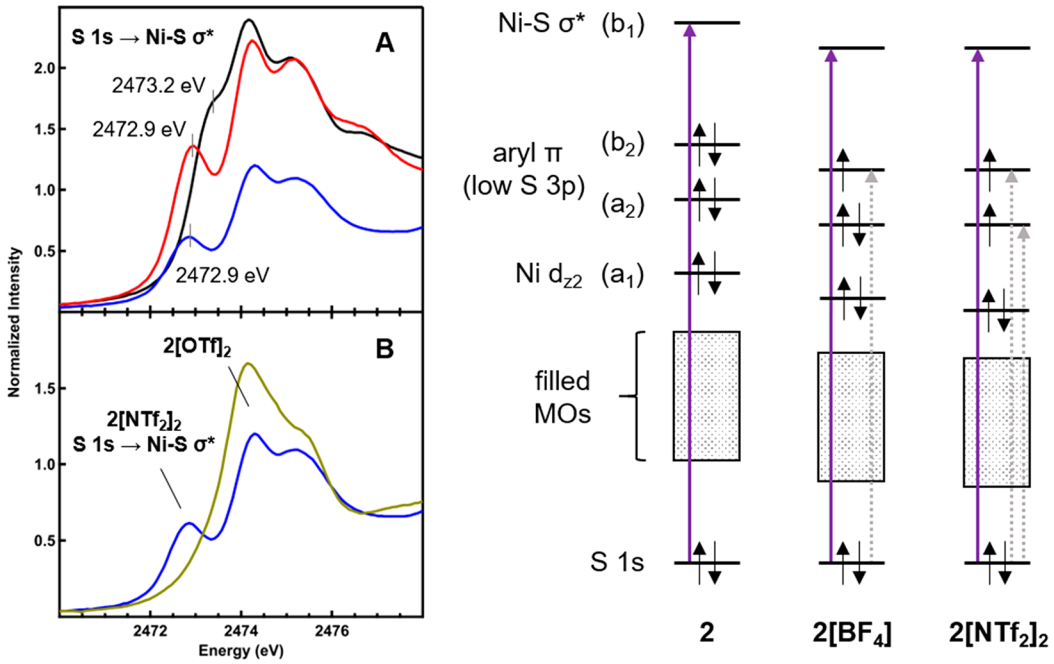

Figure 15. Top left (A): Comparison of normalized S K-edge XAS data for **2** (black), **2**[BF_4] (red), and **2**[NTf_2]$_2$ (blue). Bottom left (B): Comparison of S K-edge XAS data for **2**[NTf_2]$_2$ (blue) and **2**[OTf_2]$_2$ (gold). Right: Qualitative correlation diagram with select MOs for **2**, **2**[BF_4], and **2**[NTf_2]$_2$. MO labels correspond to those used in Figure 14.

empirical observations from our XRD and NMR studies, as well as XAS results described in the following section.

To understand the underlying relationship between the unpaired spin density and the associated electronic structure, we analyzed the calculated molecular orbitals (MOs) for **1** and **2** as a function of oxidation state and coordinating ancillary ligands. MO correlation diagrams for both series of complexes with **1** and **2** showed similar variations, and a representative MO diagram is provided by the **L2** complexes in Figure 14. Beginning with the description of closed-shell **2**, the frontier MOs most relevant to our analysis are those labeled as b_1 (LUMO), b_2 (HOMO), a_2 (HOMO−1), and a_1 (HOMO−2). MO b_1 is assigned as Ni−N and Ni−S σ^* with the Ni $3d_{xy}$, whereas the lower energy a_1 in **2** is best described as nonbonding Ni $3d_{z^2}$. MOs b_2 and a_2 are primarily ligand-centered π-orbitals with smaller amounts of Ni 3d character.

As shown in Figure 14, **2** undergoes a ligand-centered oxidation by removing an electron from the HOMO (b_2) to form **2**[BF_4]. The same occurs with **2-py**[BF_4], but the nonbonding d_{z^2} in a_1 becomes chemically engaged with pyridine in the axial coordination site. This raises the energy of the a_1 MO with respect to the HOMO and appears to account for why the EPR data for **2-py**[BF_4] and **1-py**[BF_4] begin to show electron spin on Ni in the presence of coordinating ligands, especially when cooled to 109 K.

Like the singly oxidized complexes, there are distinguishing differences in MO energies for the doubly oxidized complexes that depend on the axial coordination ability of the counteranions. Calculations on the XRD structure of **2**[NTf_2]$_2$ (i.e., no axial coordination) revealed that the second electron is removed from the ligand-centered a_2 MO to give rise to a triplet electron configuration with an ∼1 eV gap between the singly occupied α b_2 MO and the next singly occupied orbital. However, triflate coordination in **2**[OTf]$_2$ raises the energy of the a_1 MO ($3d_{z^2}$) and simultaneously decreases the energy of the b_1 MO ($3d_{xy}$). This appears to account for why the calculated spin density localizes on Ni upon axial triflate coordination, as shown in Figure 13. The two unpaired electrons are located in the metal-based b_1 and a_1 MOs in **2**[OTf]$_2$, whereas they are located in the ligand-based b_2 and a_2 MOs in **2**[NTf_2]$_2$.

Sulfur K-Edge XAS Studies. To provide a better comparison between experiment and theory using definitively known and well-defined solid-state structures, S K-edge X-ray absorption spectroscopy data were collected on solid samples of **2** and **3**, as well as oxidized salts of **2** (Figure 15). S K-edge XAS, in general, measures dipole-allowed S 1s → np transitions,[73,74] and transitions to unoccupied metal−sulfur antibonding MOs can be observed in the pre-edge region of the XAS spectra when they contain appreciable S 3p character mixing in the antibonding wave function. Notably, d^8 square planar Ni complexes with dithiolenes and other sulfur ligands have been routinely studied using S K-edge XAS to assign oxidation state and quantify related electronic structure variations.[73,75,76]

The S K-edge XAS spectra of **2** and **3** revealed only subtle differences (Figure S6), and the spectrum of **2** in Figure 15A is representative of both spectra. A pre-edge shoulder was observed at 2473.2 eV (as defined by analysis of the second derivative trace), and several higher energy features were located at 2474.1 and 2475.1 eV on top of the rising edge. The first pre-edge shoulder at 2473.2 eV was assigned as 1s → Ni−S σ^* (b_1 in Figures 14 and 15), consistent with previous studies and DFT calculations described in the previous section.[75,77] Higher energy features are assigned to transitions involving primarily ligand-based MOs containing S character. Oxidation of **2** to **2**[BF_4] caused the pre-edge feature to decrease in energy to 2472.9 eV and become more resolved with respect to the adjacent feature, consistent with the decrease in calculated b_1 MO energy in Figure 14. However, no additional pre-edge transitions are observed in the singly oxidized spectra despite the generation of an additional

DOI: 10.1021/acs.inorgchem.9b01675
Inorg. Chem. 2019, 58, 12756−12774

electron hole. This indicates that the electron was removed from an MO lacking significant S 3p character, which is corroborated by the DFT calculations that suggest the electron is removed from the ligand-based b_2 MO, as shown in Figures 14 and 15.

Further oxidation of singly oxidized **2**[BF_4] to doubly oxidized **2**[NTf_2]$_2$ yields a S K-edge XAS spectrum with the same general profile as **2**[BF_4]. The only significant difference is that the normalized pre-edge peak intensities in the spectrum of **2**[NTf_2]$_2$ are lower due to additional high-energy transitions from sulfur in the triflimidate anion that affect the data normalization (see the full spectrum in Figure S10). In contrast, the S K-edge spectrum of **2**[OTf]$_2$ reveals a significant difference when compared to **2**[NTf_2]$_2$ (Figure 15B): the pre-edge peak at 2472.9 eV in the spectrum of **2**[NTf_2]$_2$ is no longer present in the spectrum of **2**[OTf]$_2$. This feature is either pushed to higher energy, which may account for the increased intensity of the second feature at 2474.0 eV in **2**[OTf]$_2$, or the intensity is diminished by the decreased S 3p character in the associated MO. Both are plausible and can be rationalized by the axial coordination of the triflate anions. Triflate binding causes the Ni−S bonds to elongate by ca. 0.2 Å, which reflects decreased covalency in Ni−S bonds. DFT calculations are consistent with this assessment and reveal that orbital mixing between the SMe groups and the Ni $3d_{xy}$ decreases in **2**[OTf]$_2$. The α and β a_1 orbitals calculated for **2**[OTf]$_2$, which are best described as Ni−OTf σ^*, also have negligible S 3p character. Collectively, these solid-state XAS results corroborate the electronic structure variations observed in the DFT calculations.

CONCLUSION

In summary, we have described the synthesis, electrochemistry, and structures of Ni complexes with three tetradentate ligands containing flanking redox-innocent NMe_2 and SMe donor substituents. Ni complexes containing the triaryl *o*-phenylenediamine-derived ligands **L1** and **L2** revealed two fully reversible ligand-centered redox events. Metal-centered Ni^{2+}/Ni^{1+} redox couples were observed when scanning to more negative potentials and were fully reversible in **1**, whereas the SMe substituents in **2** yielded irreversible reductions and the appearance of new redox features in the CV trace. Replacing the phenylene backbone in **L2** with an ethylene linker in **L3** attenuated the reversible ligand-centered redox activity in the CV of **3**, but quasi-reversible waves were still observed, indicating that the flanking aryl groups still support some ligand-centered redox activity in the absence of the conjugated phenylene backbone. Chemically oxidizing **1** and **2** allowed the structures and electronic properties of the electrochemically generated products to be characterized by single-crystal XRD, UV-vis-NIR, NMR, EPR, and S K-edge XAS spectroscopies with different counteranions. The XRD data suggested that the redox events were primarily ligand-centered and proceed via formation of the *o*-diiminosemiquinone radical followed by the fully oxidized *o*-diiminoquinone, as is often reported for *o*-phenylenediamine and derivatives there-of.

We demonstrated how ancillary ligands with different coordinating abilities (pyridine, BF_4^-, OTf^-, and NTf_2^-) affect the electronic structure of oxidized salts of **1** and **2**. As has been observed for other Ni complexes with redox-active ligands,[58−62] treating the singly oxidized complexes **1**[BF_4] and **2**[BF_4] with excess pyridine resulted in coordination-induced valence tautomerism with the electronic structure switching from $Ni^{II}(L^{\bullet})$ to $Ni^{III}(L)$ upon pyridine binding to the metal. Similar effects were observed with BF_4^-, as shown in the low-temperature EPR spectra of **2**[BF_4]. DFT calculations showed that these experimental observations align well with recent electronic structure investigations on related square planar Co complexes[78] by revealing that axial coordination chemically engages the Ni $3d_{z^2}$ and raises the energy of the associated antibonding MO to access more Ni(III) character.

Paramagnetic NMR resonances and magnetic susceptibility data revealed the presence of unpaired spin in the doubly oxidized complexes of **1** and **2**, and DFT calculations showed how these seemingly similar open-shell electronic configurations differ depending on the identity of the coordinating anions. With bound triflate in six-coordinate **1**[OTf]$_2$ and **2**[OTf]$_2$, the complexes are best described as containing a closed-shell *o*-diiminoquinone ligand with high-spin Ni(II), whereas open shell calculations on four-coordinate **2**[NTf_2]$_2$ indicated that this complex is best described as Ni(II) with diradical character localized on the ligand. Both of these electronic configurations can be found within the various resonant forms shown in Figure 16, but they differ in that their relative weighting depends on the presence or absence of axial coordination to Ni. From the simplest perspective, axial coordination in these doubly oxidized complexes causes the ligand-centered spin density to collapse onto Ni due to reshuffling of the metal-based molecular orbitals, consistent with predictions based on ligand field theory.

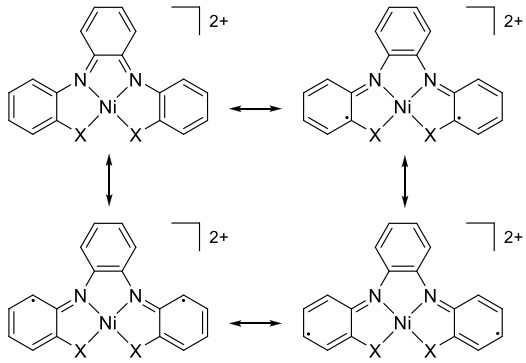

Figure 16. Selected resonance structures of doubly oxidized **1** (X = NMe_2) and **2** (X = SMe) with emphasis on structures that show how radicals can delocalize onto the flanking aryl groups.

Overall, the electronic structure studies on Ni complexes containing our triaryl tetradentate ligands with redox-innocent donor groups have revealed notable differences with respect to other complexes that either (1) lack flanking aryl groups in conjugation with the *o*-phenylenediamine backbone or (2) contain redox-noninnocent metal donor groups, such as those described by Thomas and Wieghardt (Chart 2 and Figure 8).[17,20] We anticipate that these results will provide the foundation necessary to evaluate electronic structure variations in complexes that also participate in metal−ligand cooperative binding with different substrates, as we have shown recently with Ru complexes containing **L2**.[31] The redox chemistry, ligand noninnocence, electronic structure, and reactivity of these and related complexes will be described in several forthcoming reports.

DOI: 10.1021/acs.inorgchem.9b01675
Inorg. Chem. 2019, 58, 12756−12774

EXPERIMENTAL SECTION

General Considerations. All reactions were performed under an atmosphere of N_2 or Ar using glovebox or standard Schlenk techniques, unless stated otherwise. Pentane, toluene, Et_2O, THF, MeCN, and CH_2Cl_2 were dried and degassed using a Pure Process Technologies Solvent Purification System. Benzene was distilled from sodium benzophenone and stored over 3 Å molecular sieves. Deuterated solvents were deoxygenated by three freeze−pump−thaw cycles and stored over 3 Å molecular sieves. *N,N′*-Bis[2-(methylthio)phenyl]-1,2-diaminobenzene (**L2**) was prepared as described previously.[31] All other chemicals were purchased from commercial vendors and used as received.

^{1}H, ^{13}C, and ^{11}B NMR data were recorded on a Bruker DRX-400 instrument operating at 400 MHz for ^{1}H, 100 MHz for ^{13}C, and 128 MHz for ^{11}B or on a Bruker Avance-500 instrument operating at 500 MHz for ^{1}H, 126 MHz for ^{13}C, and 470 MHz for ^{19}F. ^{19}F NMR data were collected on a Bruker Avance-300 instrument operating at 282 MHz. Chemical shifts are reported in δ units relative to residual solvent peaks (^{1}H and ^{13}C), $BF_3{\cdot}Et_2O$ (^{11}B; 0.0 ppm), or 0.05% $C_6H_5CF_3$ in C_6D_6 (^{19}F; −62.9 ppm). Microanalytical data (CHN) were collected using an EAI CE-440 Elemental Analyzer in the University of Iowa Department of Chemistry. IR spectra were acquired on a Thermo Scientific Nicolet iS5 instrument using an attenuated reflection accessory. Melting points were determined in sealed capillaries using a REACH MP device. UV−vis-NIR absorption data were collected on an Agilent Cary 5000 near-infrared spectrophotometer. HR-EI mass spectra were recorded on a Waters GCT Premier Instrument using TOF. Fragment ions (M, molecule; L, ligand) were assigned based on comparison to calculated natural abundance isotopic distributions.

N,N′-Bis[2-(N,N-dimethylamine)phenyl]-1,2-diaminobenzene, H_2(^{Me}NNNN^{Me})-DAB, ***L1****.* $Pd_2(dba)_3$ (1.70 g, 1.85 mmol), *rac*-BINAP (1.73 g, 2.80 mmol, 7.5 mol %), NaO^{t}Bu (10.67 g, 111.0 mmol), degassed water (1.0 mL), and *o*-phenylenediamine (4.0 g, 37.0 mmol) were added to dry toluene (250 mL). The reaction mixture was heated to reflux under N_2, and a solution of 2-bromo-*N,N′*-dimethylaniline (14.8 g, 74.0 mmol, 10.7 mL) in toluene (50 mL) was added dropwise over 6 h. The reaction was heated to reflux for 72 h under a N_2 atmosphere. After cooling to RT, the mixture was treated with a saturated aqueous solution of NH_4Cl immediately upon being exposed to air. The mixture was filtered through a pad of Celite and washed with toluene until the filtrate was colorless. The organic phase was separated, concentrated under reduced pressure, and purified by column chromatography on 70−230 mesh silica gel (2:98 Et_2O/hexane) to afford a yellow/white solid. The solid was recrystallized from MeCN to afford colorless blocks. Yield: 7.94 g (62%). Mp: 91−94 °C. Anal. Calcd for $C_{22}H_{26}N_4$: C, 76.26; H, 7.56; N, 16.17. Found: C, 76.33 H, 7.46; N, 16.03. HR-EIMS (70 eV) *m/z*: [M] calcd for $C_{22}H_{26}N_4$ 346.215; found 346.218. ^{1}H NMR (400 MHz, $CDCl_3$): δ 2.58 (s, 12H, N−CH_3), 6.65 (br s, 2H, N−H), 6.80 (td, J = 1.6 Hz, J = 7.6 Hz, 2H, Ar−H), 6.95 (t, J = 7.4, 2H, Ar−H), 7.00 (dd, J = 3.3 Hz, J = 6.0 Hz, 2H, Ar−H), 7.05 (d, J = 8.5 Hz, 2H, Ar−H), 7.08 (dd, J = 1.1 Hz, J = 7.8 Hz, 2H, Ar−H), 7.38 (dd, J = 3.6 Hz, J = 5.8 Hz, 2H, Ar−H). ^{13}C NMR (100 MHz, $CDCl_3$): δ 44.16 (N−$\underline{C}H_3$), 114.14 (Ar−C). 119.50 (Ar−C), 119.78 (Ar−C), 120.50 (Ar−C), 122.80 (Ar−C), 124.38 (Ar−C), 135.19 (Ar−C), 139.11 (Ar−C), 142.39 (Ar−C). IR (KBr, cm^{-1}): 3318 m, 3267 m, 3037 m, 2981 m, 2940 m, 2863 w, 2824 m, 2784 m, 1588 s, 1526 s, 1503 s, 1491 m, 1451 m, 1433 m, 1410 m, 1333 m, 1289 s, 1275 s, 1211 w, 1182 m, 1153 s, 1111 m, 1092 m, 1043 s, 941 s, 900 vw, 850 vw, 737 s.

N,N′-Bis[2-(methylthio)phenyl]-1,2-diaminoethane, H_2(^{Me}SNNS^{Me})-DAE, ***L3****.* 2-(Methylthio)aniline (14.0 g, 100 mmol, 12.6 mL) was added to methanol (50 mL) in air. The mixture was heated to reflux, and 40% glyoxal in water (4.0 g, 69.0 mmol, 7.8 mL) was added dropwise. The reaction mixture was heated to reflux for 2 h, which caused slow formation of an orange precipitate. The reaction mixture was cooled to 0 °C, and the orange solid was collected by filtration. Recrystallization from boiling pyridine yielded orange needles of *N,N′*-bis[2-(methylthio)phenyl]-ethanediylidene. Yield: 13.1 g (43%). ^{1}H NMR (400 MHz, $CDCl_3$): δ 2.49 (s, 6H, S−CH_3), 7.09 (dd, J = 1.21 Hz, J = 7.9 Hz, 2H, Ar−H), 7.18 (td, J = 1.5 Hz, J = 7.8 Hz, 2H, Ar−H), 7.27 (m, 4H, Ar−H), 8.43 (s, 2H, N=CH). *N,N′*-Bis[2-(methylthio)phenyl]ethanediylidene was dried over P_2O_5 for 12 h before proceeding to the next step.

N,N′-bis[2-(methylthio)phenyl]ethanediylidene (13.0 g, 43.3 mmol) was dissolved in THF (250 mL) under an atmosphere of N_2 and cooled to −10 °C. $NaBH_4$ (3.27 g, 86.5 mmol) in THF (50 mL) was added dropwise over 30 min. The reaction mixture was allowed to slowly warm to RT. The yellow/orange solution slowly turned colorless, and a small amount of effervescence was observed. The mixture was stirred for 12 h and then evaporated to dryness under a vacuum to reveal a white solid that immediately turned yellow upon exposure to air. The yellow solid was dissolved in CH_2Cl_2 and washed with DI water. Recrystallization from CH_2Cl_2 resulted in yellow blocks of **L3**. Yield: 11.1 g (84%). Mp: 77−80 °C. ^{1}H NMR (400 MHz, $CDCl_3$): δ 2.30 (s, 6H, S−CH_3), 3.51 (s, 4H, N−CH_2), 5.37 (br s, 2H, N−H), 6.66−6.73 (m, 4H, Ar−H), 7.20 (td, J = 1.7 Hz, J = 7.9 Hz, 2H, Ar−H), 7.41 (dd, J = 1.5 Hz, J = 8.1 Hz, 2H, Ar−H). ^{13}C NMR (100 MHz, $CDCl_3$): δ 18.28 (S−$\underline{C}H_3$), 43.13 (N−$\underline{C}H_2$), 110.38 (Ar−C), 117.67 (Ar−C), 120.49 (Ar−C), 129.61 (Ar−C), 134.37 (Ar−C), 148.01 (Ar−C). IR (ATR, cm^{-1}): 3326 m, 3057 m, 3017 vw, 2988 vw, 2958 vw, 2918 m, 2845 m, 1916 w, 1876 w, 1837 vw, 1580 s, 1494 vs, 1482 s, 1449 s, 1429 s, 1309 s, 1282 m, 1240 s, 1214 m, 1172 w, 1135 m, 1088 w, 1037 s, 965 m, 956 m, 919 m, 839 w, 821 m, 747 vs, 737 vs, 717 s, 692 m.

Ni(^{Me}NNNN^{Me})-DAB, ***1****.* A 50 mL Schlenk flask was charged with $NiBr_2$ (0.379 g, 1.73 mmol) and **L1** (0.600 g, 1.73 mmol) in 25 mL of THF. The reaction was heated to reflux overnight, and a mint green solid slowly formed. After cooling to RT, the mixture was filtered and the solid was washed with Et_2O (3 × 20 mL). A solution of NaO^{t}Bu (0.333 g, 3.46 mmol) in THF (25 mL) was transferred via cannula into the Schlenk flask containing the solid. The color immediately turned dark green/brown, and the mixture was stirred for 12 h. The mixture was filtered, and the remaining gray precipitate was washed with THF (3 × 10 mL). The combined filtrate and washings were evaporated to dryness under a vacuum to yield a dark green solid. Cooling concentrated THF solutions or layering with Et_2O yielded single crystals. Yield: 0.42 g (60%). Anal. Calcd for $C_{22}H_{24}N_4Ni$: C, 65.54; H, 6.00; N, 13.90. Found: C, 65.66; H, 5.88; N, 13.68. Mp: >250 °C. EI-HRMS (70 eV) *m/z*: [M] calcd for $C_{22}H_{24}N_4Ni$ 402.135; found 402.136. ^{1}H NMR (400 MHz, THF-d_8): δ 3.05 (s, 12H, N−CH_3), 6.27 (t, J = 7.2 Hz, 2H, Ar−H), 6.34 (dd, J = 3.0 Hz, J = 6.2 Hz, 2H, Ar−H), 6.85 (t, J = 7.5 Hz, 2H, Ar−H), 7.05 (d, J = 8.2 Hz, 2H, Ar−H), 7.18 (dd, J = 3.7 Hz, J = 6.0 Hz, 2H, Ar−H), 7.44 (d, J = 8.1 Hz, 2H, Ar−H). ^{13}C NMR (100 MHz, THF-d_8): δ 50.34 (N−$\underline{C}H_3$), 113.27 (Ar−C), 114.05 (Ar−C), 114.24 (Ar−C), 116.52 (Ar−C), 119.47 (Ar−C), 128.60 (Ar−C), 147.24 (Ar−C), 147.78 (Ar−C), 149.58 (Ar−C). IR (ATR, cm^{-1}): 3049 w, 3008 w, 2977 w, 2917 w, 1591 m, 1572 w, 1550 m, 1480 s, 1436 m, 1396 w, 1359 s, 1323 m, 1294 m, 1276 m, 1239 w, 1208 m, 1179 m, 1135 w, 1113 w, 1090 w, 1061 w, 1041 m, 991 m, 923 m, 902 w, 883 m, 867 w, 833 w, 784 vw, 749 m, 739 m, 718 s. UV−vis (CH_2Cl_2): 210 nm (ε = 63700 M^{-1} cm^{-1}), 278 nm (ε = 17300 M^{-1} cm^{-1}), 355 nm (ε = 29400 M^{-1} cm^{-1}), 557 nm (ε = 344 M^{-1} cm^{-1}), 702 nm (ε = 409 M^{-1} cm^{-1}).

Ni(^{Me}SNNS^{Me})-DAB, ***2****.* A 25 mL Schlenk flask was charged with $NiBr_2$ (0.186 g, 0.85 mmol), **L2** (0.300 g, 0.85 mmol), and THF (12 mL). The mixture was heated to reflux for 12 h, resulting in a mint green precipitate. After cooling to RT, the mixture was filtered and the green solid was washed with Et_2O (3 × 20 mL). A solution of NaO^{t}Bu (0.164 g, 1.7 mmol) in THF (20 mL) was transferred via cannula into the Schlenk flask containing the solid. The color immediately changed to dark green, and the mixture was stirred overnight. The mixture was filtered, and the remaining gray precipitate was washed with THF (3 × 10 mL). The combined filtrate and washings were evaporated to dryness under a vacuum to reveal a tacky, dark green solid. Single crystals of **2** were grown by vapor diffusion with benzene/Et_2O. Yield: 0.19 g (54%). Anal. Calcd for $C_{20}H_{18}N_2NiS_2$: C, 58.70; H, 4.43; N, 6.85. Found: C, 58.89; H, 4.40; N, 6.84. Mp: 171 °C. EI-HRMS (70 eV) *m/z*: [M] calcd for

DOI: 10.1021/acs.inorgchem.9b01675
Inorg. Chem. 2019, 58, 12756−12774

$C_{20}H_{18}N_2NiS_2$ 408.026; found 408.029. ^{1}H NMR (500 MHz, C_6D_6): δ 1.71 (s, 6H, S−CH_3), 6.39 (td, J = 1.0 Hz, J = 7.2 Hz, 2H, Ar−H), 6.79 (dd, J = 1.4 Hz, J = 7.6 Hz, 2H, Ar−H), 6.88 (dd, J = 3.3 Hz, J = 6.0 Hz, 2H, Ar−H), 6.99 (td, J = 1.5 Hz, J = 7.8 Hz, 2H, Ar−H), 7.80 (d, J = 8.5 Hz, 2H, Ar−H), 7.84 (dd, J = 3.4 Hz, J = 5.9 Hz, 2H, Ar−H). ^{13}C NMR (126 MHz, C_6D_6): δ 24.16 (S−CH_3), 114.36 (Ar−C), 115.50 (Ar−C), 115.71 (Ar−C), 118.52 (Ar−C), 120.83 (Ar−C), 131.38 (Ar−C), 132.05 (Ar−C), 147.67 (Ar−C), 156.03 (Ar−C). IR (ATR, cm^{-1}): 3045 w, 3012 w, 2914 vw, 1581 m, 1560 m, 1544 m, 1476 s, 1455 vs, 1432 s, 1410 m, 1345 m, 1330 s, 1300 s, 1239 m, 1206 m, 1172 w, 1153 w, 1124 w, 1045 w, 1033 m, 1026 m, 961 m, 918 m, 730 vs. UV−vis (CH_2Cl_2): 215 nm (ε = 108000 M^{-1} cm^{-1}), 230 nm (ε = 82900 M^{-1} cm^{-1}), 295 nm (ε = 46800 M^{-1} cm^{-1}), 349 nm (ε = 53600 M^{-1} cm^{-1}), 598 nm (ε = 475 M^{-1} cm^{-1}), 796 nm (ε = 366 M^{-1} cm^{-1}).

*Ni(^{Me}SNNS^{Me})-DAE, **3**.* A 25 mL Schlenk flask was charged with $NiBr_2$ (0.215 g, 0.99 mmol), **L3** (0.300 g, 0.99 mmol), and THF (12 mL). The reaction was heated to reflux overnight, resulting in a mint green precipitate the next day. After cooling to RT, the mixture was filtered and the mint green solid was washed with Et_2O (3 × 20 mL). A solution of NaO^{t}Bu (0.189 g, 1.97 mmol) in THF (20 mL) was transferred via cannula into the Schlenk flask containing the solid. The color immediately turned blue, and the mixture was stirred overnight. The blue mixture was filtered, and the remaining gray solid was washed with THF (3 × 10 mL). The combined filtrate and washings were evaporated to dryness under a vacuum to yield a dark blue/green solid. The solid was dissolved in benzene and layered with Et_2O to yield single crystals. Yield: 0.15 g (42%). Anal. Calcd for $C_{16}H_{18}N_2NiS_2$: C, 53.21; H, 5.02; N, 7.76. Found: C, 53.25; H, 4.90; N, 7.61. Mp: 180−182 °C. EI-HRMS (70 eV) m/z: [M] calcd for $C_{16}H_{18}N_2NiS_2$ 360.026; found 360.024. ^{1}H NMR (400 MHz, C_6D_6): δ 1.88 (s, 6H, S−CH_3), 3.33 (br s, 4H, N−CH_2), 6.40 (t, J = 7.1 Hz, 2H, Ar−H), 6.50 (d, J = 8.3 Hz, 2H, Ar−H), 6.86 (d, J = 7.3 Hz, 2H, Ar−H), 7.11 (t, J = 7.5 Hz, 2H, Ar−H). ^{13}C (100 MHz, C_6D_6): δ 24.56 (S−CH_3), 54.53 (N−CH_2), 111.12 (Ar−C), 112.74 (Ar−C), 116.88 (Ar−C), 131.70 (Ar−C), 132.12 (Ar−C), 162.00 (Ar−C). IR (ATR, cm^{-1}): 3197 m, 3123 s, 2964 s, 2933 s, 2877 m, 1577 w, 1480 m, 1460 w, 1445 s, 1407 s, 1342 m, 1283 m, 1200 w, 1178 m, 1137 m, 1067 s, 1048 w, 1033 w, 1018 s, 976 vs, 955 s, 888 w, 868 w, 801 m, 770 vs, 762 vs, 737 s, 708 w, 672 m. UV−vis (CH_2Cl_2): 240 nm (ε = 40700 M^{-1} cm^{-1}), 284 nm (ε = 23900 M^{-1} cm^{-1}), 330 nm (ε = 16300 M^{-1} cm^{-1}), 390 nm (ε = 6720 M^{-1} cm^{-1}), 667 nm (ε = 1170 M^{-1} cm^{-1}).

*[Ni(^{Me}NNNN^{Me})-DAB][BF$_4$], **1[BF$_4$]**.* A slurry of $AgBF_4$ (0.024 g, 0.120 mmol) in CH_2Cl_2 (5 mL) was added dropwise to a stirring solution of **1** (0.050 g, 0.120 mmol) in CH_2Cl_2 (10 mL). The color immediately turned dark purple. The mixture was stirred for 30 min and filtered through Celite. Layering the concentrated filtrate with Et_2O resulted in dark green needles. Yield: 0.041 g (68%). Anal. Calcd for $C_{22}H_{24}BF_4N_4Ni$: C, 53.93; H, 4.94; N, 11.44. Found: C, 53.78; H, 5.14; N, 11.07. Mp: >250 °C. HR-EIMS (70 eV) m/z: [M−BF_4]$^+$ calcd for $C_{22}H_{24}N_4Ni$ 402.135; found 402.142. ^{11}B NMR (128 MHz, CD_2Cl_2): δ −1.36. ^{19}F NMR (282 MHz, CD_2Cl_2): δ −151.63. IR (ATR, cm^{-1}): 2964 m, 2878 w, 2687 vw, 1591 vw, 1579 vw, 1563 w, 1528 w, 1483 m, 1428 s, 1367 m, 1335 s, 1297 m, 1284 m, 1203 w, 1190 w, 1175 w, 1158 m, 1096 m, 1007 m, 1031 vs, 958 s, 926 m, 910 m, 875 s, 854 m, 841 m, 814 m, 739 s, 717 s, 691 s, 651 s. UV−vis-NIR (CH_2Cl_2): 279 nm (ε = 13900 M^{-1} cm^{-1}), 395 nm (ε = 13200 M^{-1} cm^{-1}), 548 nm (ε = 2690 M^{-1} cm^{-1}), 584 nm (ε = 2580 M^{-1} cm^{-1}), 1130 nm ((ε = 1400 M^{-1} cm^{-1}), 1335 (ε = 2300 M^{-1} cm^{-1}), 1666 nm (ε = 2400 M^{-1} cm^{-1}).

*[Ni(^{Me}SNNS^{Me})-DAB][BF$_4$], **2[BF$_4$]**.* Prepared using the same procedure described for **1**[BF_4] with **2** (0.050 g, 0.122 mmol) and $AgBF_4$ (0.024 g, 0.122 mmol). Yield: 0.031 g (52%). Anal. Calcd for $C_{20}H_{18}BF_4N_2NiS_2$: C, 48.43; H, 3.66; N, 5.65. Found: C, 48.07; H, 3.84; N, 5.36. Mp: 219−221 °C. ^{11}B NMR (128 MHz, CD_2Cl_2): δ −1.12. ^{19}F NMR (282 MHz, CD_2Cl_2): δ −149.48. IR (ATR, cm^{-1}): 3056 w, 2965 m, 2935 m, 2878 w, 1578 vw, 1558 w, 1531 m, 1462 m, 1420 s, 1357 m, 1312 s, 1272 m, 1219 w, 1196 m, 1173 m, 1157 m, 1029 vs, 974 s, 920 m, 875 m, 858 m, 740 vs, 716 s, 702 m, 663 m, 640 s, 631 m, 590 m. UV−vis-NIR (CH_2Cl_2): 229 nm (ε = 21300 M^{-1} cm^{-1}), 255 nm (ε = 20400 M^{-1} cm^{-1}), 286 nm (sh, ε = 15700 M^{-1} cm^{-1}), 398 nm (ε = 11000 M^{-1} cm^{-1}), 547 nm (ε = 2770 M^{-1} cm^{-1}), 1150 nm (ε = 970 M^{-1} cm^{-1}), 1373 nm (ε = 1580 M^{-1} cm^{-1}), 1689 nm (ε = 1470 M^{-1} cm^{-1}).

*[Ni(^{Me}NNNN^{Me})-DAB][NTf$_2$], **1[NTf$_2$]**.* Prepared using the same procedure described for **1**[BF_4] with **1** (0.050 g, 0.120 mmol) and $AgNTf_2$ (0.047 g, 0.120 mmol). Yield: 0.056 g (67%). Anal. Calcd for $C_{24}H_{24}F_6N_5NiO_4S_2$: C, 42.19; H, 3.54; N, 10.25. Found: C, 42.81; H, 3.25; N, 10.04. ^{19}F NMR (282 MHz, CH_2Cl_2): δ −78.19. UV−vis-NIR (CH_2Cl_2): 211 nm (ε = 42500 M^{-1} cm^{-1}), 238 nm (sh, ε = 22400 M^{-1} cm^{-1}), 280 nm (ε = 20500 M^{-1} cm^{-1}), 399 nm (ε = 19700 M^{-1} cm^{-1}), 496 nm (sh, ε = 2900 M^{-1} cm^{-1}), 583 nm (ε = 4000 M^{-1} cm^{-1}), 1124 nm (ε = 2000 M^{-1} cm^{-1}), 1340 nm (ε = 3580 M^{-1} cm^{-1}), 1663 nm (ε = 3900 M^{-1} cm^{-1}).

*[Ni(^{Me}SNNS^{Me})-DAB][NTf$_2$], **2[NTf$_2$]**.* Prepared using the same procedure described for **1**[BF_4] with **2** (0.050 g, 0.122 mmol) and $AgNTf_2$ (0.047 g, 0.122 mmol). Yield: 0.069 g (83%). Anal. Calcd for $C_{22}H_{18}F_6N_3NiO_4S_4$: C, 38.33; H, 2.63; N, 6.10. Found: C, 38.32; H, 2.20; N, 5.99. ^{19}F NMR (282 MHz, CH_2Cl_2): δ −78.79. UV−vis-NIR (CH_2Cl_2): 210 nm (ε = 42000 M^{-1} cm^{-1}), 258 nm (ε = 19500 M^{-1} cm^{-1}), 289 nm (ε = 19600 M^{-1} cm^{-1}), 399 nm (ε = 11900 M^{-1} cm^{-1}), 547 nm (ε = 3100 M^{-1} cm^{-1}), 1150 nm (ε = 940 M^{-1} cm^{-1}), 1373 nm (ε = 1500 M^{-1} cm^{-1}), 1692 nm (ε = 1350 M^{-1} cm^{-1}).

*[Ni(^{Me}NNNN^{Me})-DAB][OTf]$_2$, **1[OTf]$_2$**.* AgOTf (0.064 g, 0.248 mmol) was added to a stirring solution of **1** (0.050 g, 0.120 mmol) in CH_2Cl_2 (10 mL). The color turned purple and then slowly dark red. The reaction mixture was stirred for 30 min and then filtered through Celite. Layering the CH_2Cl_2 filtrate with Et_2O resulted in gold blocks. Yield: 0.053 (60%). Anal. Calcd for $C_{24}H_{24}F_6N_4NiO_6S_2$: C, 41.10; H, 3.45; N, 7.99. Found: C, 40.81; H, 3.31; N, 7.67. Mp: >250 °C. HR-EIMS (70 eV) m/z: [M−2OTf]$^{2+}$ calcd for $C_{22}H_{24}N_4Ni$ 402.135; found 402.129. ^{1}H NMR (500 MHz, CD_2Cl_2): δ 2.40, 3.01, 12.73, 14.94, 21.13, 39.44. ^{19}F NMR (470 MHz, CD_2Cl_2): −38.5. IR (ATR, cm^{-1}): 3376 vw, 2965 w, 1585 w, 1571 w, 1536 w, 1477 m, 1455 w, 1432 w, 1324 w, 1296 vs, 1230 vs, 1211 vs, 1175 vs, 1147 s, 1100 m, 1036 s, 1020 vs, 917 s, 875 m, 858 w, 843 w, 823 m, 767 vs, 741 s, 678 s. UV−vis (CH_2Cl_2): 251 nm (ε = 12000 M^{-1} cm^{-1}), 546 nm (ε = 9550 M^{-1} cm^{-1}), 581 nm (ε = 9590 M^{-1} cm^{-1}).

*[Ni(^{Me}SNNS^{Me})-DAB][OTf]$_2$, **2[OTf]$_2$**.* AgOTf (0.063 g, 0.244 mmol) was added to a stirring solution of **2** (0.050 g, 0.122 mmol) in CH_2Cl_2 (10 mL). The color turned purple and then eventually to dark blue. The mixture was stirred for 30 min and then filtered through Celite. Layering the filtrate with Et_2O resulted in gold blocks. Yield: 0.048 g, (56%). Anal. Calcd for $C_{22}H_{18}F_6N_2NiO_6S_4{\cdot}CH_2Cl_2$: C, 34.87; H, 2.54; N, 3.54. Found: C, 34.61; H, 2.59; N, 3.76. Mp: >250 °C. ^{1}H NMR (400 MHz, CD_2Cl_2): δ 1.85, 3.69, 4.30, 8.13, 25.34, 26.37, 35.97. ^{19}F NMR (282 MHz, CD_2Cl_2): δ −41.7. IR (ATR, cm^{-1}): 3092 vw, 3086 vw, 3029 vw, 1578 w, 1531 w, 1460 w, 1431 m, 1398 w, 1330 m, 1311 s, 1302 s, 1262 w, 1230 s, 1205 vs, 1159 vs, 1136 s, 1059 m, 1025 m, 1014 vs, 980 s, 974 s, 825 m, 799 m, 766 s, 760 vs, 724 m, 716 s, 663 m, 665 m, 633 vs. UV−vis (CH_2Cl_2): 230 nm (ε = 28400 M^{-1} cm^{-1}), 255 nm (ε = 25800 M^{-1} cm^{-1}), 414 nm (ε = 5500 M^{-1} cm^{-1}), 581 nm (ε = 14200 M^{-1} cm^{-1}), 604 nm (ε = 14000 M^{-1} cm^{-1}).

*[Ni(^{Me}SNNS^{Me})-DAB][NTf$_2$]$_2$, **2[NTf$_2$]$_2$**.* $AgNTf_2$ (0.095 g, 0.244 mmol) was added to a stirring solution of **2** (0.050 g, 0.122 mmol) in CH_2Cl_2 (10 mL). The color turned purple and then slowly to dark blue-red. The mixture was stirred for 30 min and filtered through Celite. Layering the filtrate with Et_2O yielded green needles. Yield: 0.100 g (86%). Anal. Calcd for $C_{24}H_{18}F_{12}N_4NiO_8S_6$: C, 29.73; H, 1.87; N, 5.78. Found: C, 29.78; H, 1.60; N, 5.70. Mp: 140−142 °C. ^{1}H NMR (400 MHz, CD_2Cl_2): δ 5.66, 6.65, 8.04, 15.77. ^{19}F NMR (282 MHz, CD_2Cl_2): −72.18. IR (ATR, cm^{-1}): 3121 vw, 3083 vw, 3054 vw, 2965 w, 2878 vw, 1574 m 1529 w, 1510 vw, 1464 m, 1431 m, 1394 m, 1384 m, 1336 s, 1325 s, 1315 s, 1226 m, 1196 s, 1179 vs, 1126 vs, 1055 s, 980 m, 966 m, 957 m, 884 w, 854 m, 787 s, 775 s, 765 vs, 736 s, 719 m, 651 s. UV−vis (CH_2Cl_2): 258 nm (ε = 21200

DOI: 10.1021/acs.inorgchem.9b01675
Inorg. Chem. 2019, 58, 12756−12774

M^{-1} cm^{-1}), 405 nm (ε = 5580 M^{-1} cm^{-1}), 598 nm (ε = 8520 M^{-1} cm^{-1}).

Single-Crystal X-ray Diffraction Studies. Single crystals retrieved from acetonitrile [H_2(^{Me}NNNN^{Me})-DAB, **L1**], THF/Et_2O (**1**), benzene/Et_2O (**2** and **3**), and CH_2Cl_2/Et_2O (**1**[BF_4], **1**[OTf]$_2$, **2**[BF_4], **2**[NTf_2]$_2$, and **2**[OTf]$_2$) were mounted on a MiTeGen micromount with ParatoneN oil. The data were collected on a Bruker Nonius Kappa CCD, with an Apex II charge-coupled-device (CCD) detector (**L1**, **1**[OTf]$_2$, **2**, **2**[NTf_2]$_2$, and **2**[OTf]$_2$), or on a Nonius Kappa CCD difractometer (**1**, **1**[BF_4], and **2**[BF_4]). The samples were cooled to 190(1) K by an Oxford Cryostreams 700 low-temperature device. Both instruments were equipped with a graphite monochromatized Mo Kα X-ray source (λ = 0.71073). A hemisphere of data were collected using phi and omega scans. Data collection, initial indexing, and cell refinement were conducted using the Bruker Apex II suite (Bruker Nonius Kappa CCD) or using COLLECT and DENZO/SCALEPACK[79] (Nonius Kappa CCD). The data were corrected for absorption using redundant reflections and the SADABS program.[80] Structures were solved by direct methods and difference Fourier techniques performed in Olex2.[81] Hydrogen atom positions were idealized and allowed to ride on the attached carbon or nitrogen atoms, with exception of **1**, **1**[BF_4], **2**, and **2**[BF_4] where close contact hydrogen atoms of the aryl groups were allowed to refine. A solvent mask was applied to the refinement of **2**[NTf_2]$_2$ to account for disordered solvent in the crystal lattice that could not be modeled satisfactorily.[82] Disordered counteranions of **1**[BF_4], **2**[BF_4], and **2**[OTf]$_2$ were modeled upon locating the second orientation, and the two sites were summed together with a site-occupancy factor (SOF) set at 1.0. The displacement parameters of the disordered components were constrained to produce satisfactory ellipsoids. *HKL* reflections with error/esd values ±10 were omitted from the models. The final refinement included anisotropic temperature factors on all non-hydrogen atoms. Structure solution and refinement were performed in Olex2[81] using SHELXT[83] and SHELXL.[84] Publication figures were generated using Mercury CSD 3.10.[85] Data collection and refinement details are listed in Tables S1 and S2.

Electrochemical Studies. Cyclic voltammetry (CV) experiments were performed under a N_2 atmosphere in a Genesis glovebox using a CH Instruments CHI660D potentiostat. The electrochemical cell was purged in the glovebox for 45 min with ultrahigh-purity (UHP) Ar (99.999%) before each CV experiment was performed. The electrolyte was 0.1 M (^{n}Bu_4N)PF_6 (Aldrich, ≥99.0%) in THF with an analyte concentration of 1 mM. The electrochemical cell consisted of a glassy carbon working electrode with a platinum wire used as the counter and quasi reference electrodes. All potentials are reported versus the Fc^+/Fc redox couple, measured by adding a small amount (~0.005 M) of ferrocene to the electrochemical solutions at the end of each series of measurements.

EPR Studies. X-Band EPR spectra were recorded on a Bruker EMX EPR spectrometer equipped with a flow-through cryostat in conjunction with a Eurotherm B-VT-2000 controller. Samples were measured in 4 mm O.D. quartz tubes featuring J-Young tops. For low-temperature measurements, samples were slowly frozen by dipping the EPR tube containing the sample in and out of liquid nitrogen until frozen and then quickly transferred into the EPR cavity.

All EPR simulations were performed in MATLAB (2018b) using the Easyspin (v5.2.25) toolbox and utilizing the least-squares fit function (esfit).[86,87] Spectra of the singly oxidized complexes that contained a single species were initially fit by manually finding g values for an S = 1/2 spin system containing ^{14}N and ^{1}H nuclei. Upon satisfactory agreement to the experimental spectra, esfit was used to optimize the g values and A hyperfine terms. Spectra that contained multiple species were fit by separately modeling each species as an S = 1/2 spin system. Once esfit found a best fit solution for each species, a weighting term (Sys.weight) was added and manually adjusted to match the weighting observed in the experimental spectrum. The esfit function was again allowed to refine to yield the final g values, A hyperfine terms, and weighting terms for the two species. Simulations for the EPR spectrum of **2**[BF_4] collected in 2-MeTHF/DCM at 109 K were conducted in a similar fashion using a third S = 1/2 spin system to account for spin localization on the ^{19}F atom.

The doubly oxidized compounds were modeled as an S = 1 spin system with added D and E zero field splitting parameters. Initial fitting followed the same procedure as described above for the singly oxidized compounds. Upon satisfactory agreement to the experimental data with initial fits, esfit was allowed to refine to find g values, A hyperfine terms, and D and E zero field splitting parameters with the best fit.

X-ray Absorption Spectroscopy Studies. All XAS data were collected at the Stanford Synchrotron Radiation Lightsource (SSRL). Solid samples were prepared air-sensitively as reported previously.[88−93] S K-edge XAS data were collected on Beamline (BL) 4-3, which is equipped with a 20-pole, 2.0 T wiggler and a double-crystal monochromator cooled with liquid nitrogen. The sample chambers at each beamline were maintained under a He atmosphere at room temperature, and fluorescence was measured using a PIPS detector. Data were collected in triplicate scans for each sample during each run, and a calibration scan was collected before and after each sample set on a $Na_2S_2O_3$ standard with the first pre-edge set to 2472.02 eV.[77] Spectra were collected using energy step sizes of 1.0, 0.8, and 1.5 eV, over the pre-edge (2380−2465 eV), edge (2465−2490 eV), and post-edge (2490−2690 eV) regions, respectively.

All calibrations, background subtractions, normalizations, and averaging were performed using the Athena program in the IFFEFIT XAS software package as previously reported.[94,95] The background was removed from each spectrum by fitting a first order polynomial to the pre-edge region. The data were normalized by fitting the post-edge region with a first or second order polynomial and setting the step function to an intensity of 1.0 at a set point of 2490 eV.

Density Functional Theory Calculations. Unrestricted Kohn−Sham density functional theory calculations were performed using the QCHEM 5.1 package using a B3LYP/6-31G(d,p) functional/basis set combination. Each single-molecule calculation was performed on isolated molecules in the gas phase, neglecting any contribution from the solvent or crystal lattice. Each complex was built starting from XRD geometry data in order to more reasonably represent the molecules seen in experiment; preliminary investigations indicated several close-in-energy minima from subtle rotations of the benzene rings.

Since geometry optimization resulted in a slight puckering of the rings, we tested the sensitivity of the excess spin density localization to the precise geometry involved. The localization was observed in a fashion that was independent of several geometries (i.e., free drawn optimization, XRD structure, and XRD structure plus geometry optimization) except for **2**[NTf_2]$_2$, which shows differences in NTf_2^- binding to the metal (as described in the text). The calculation is not sensitive to functional. PBE0 and M06 both show localization on the nickel for the **2**[OTf]$_2$, and PBE0 shows localization for **1**[OTf]$_2$. Spin density calculations showed no obvious dependence on the basis set selected, and spin density differences were ultimately calculated using the 6-31G(d,p) basis set. Finally, unrestricted Kohn−Sham calculations were performed on the structures of square planar (neutral, singlet) metal complexes **1** and **2**, as a negative control. As expected, these structures did not show any spin density difference.

■ ASSOCIATED CONTENT

Supporting Information

The Supporting Information is available free of charge on the ACS Publications website at DOI: 10.1021/acs.inorgchem.9b01675.

Tabulated crystallographic data, molecular structures, and spectroscopic data (NMR, UV−vis, EPR, and S K-edge XAS). Bond distances and angles from DFT calculations (PDF)

DOI: 10.1021/acs.inorgchem.9b01675
Inorg. Chem. 2019, 58, 12756−12774

Accession Codes

CCDC 1919326−1919334 contain the supplementary crystallographic data for this paper. These data can be obtained free of charge via www.ccdc.cam.ac.uk/data_request/cif, or by emailing data_request@ccdc.cam.ac.uk, or by contacting The Cambridge Crystallographic Data Centre, 12 Union Road, Cambridge CB2 1EZ, UK; fax: + 44 1223 336033.

AUTHOR INFORMATION

Corresponding Authors

*E-mail: scott-daly@uiowa.edu.
*E-mail: scott-k-shaw@uiowa.edu.
*E-mail: james-shepherd@uiowa.edu.

ORCID

Suzanne C. Bart: 0000-0002-8918-9051
Scott K. Shaw: 0000-0003-3767-3236
James J. Shepherd: 0000-0002-6164-485X
Scott R. Daly: 0000-0001-6229-0822

Notes

The authors declare no competing financial interest.

ACKNOWLEDGMENTS

This work was generously supported by the National Science Foundation (1650894 and 1651381). We thank Dale Swenson for collecting the single-crystal XRD data. We also would like to thank Bruker for collecting and solving the single-crystal XRD data for **3**. C.M.D. would like to thank the U.S. Department of Education for a Graduate Assistance in Areas of National Need (GAANN) fellowship. Portions of this research were carried out at the Stanford Synchrotron Radiation Laboratory (SSRL), which is a national user facility supported by the US Department of Energy, Office of Science, Office of Basic Energy Sciences under contract number DE-AC02-76SF00515. We thank Erik Nelson and Matthew Latimer for their assistance with the S K-edge XAS measurements at SSRL.

REFERENCES

(1) Chirik, P. J. Preface: Forum on redox-active ligands. *Inorg. Chem.* **2011**, *50*, 9737−9740.
(2) Storr, T.; Mukherjee, R. Preface for the forum on applications of metal complexes with ligand-centered radicals. *Inorg. Chem.* **2018**, *57*, 9577−9579.
(3) Luca, O. R.; Crabtree, R. H. Redox-active ligands in catalysis. *Chem. Soc. Rev.* **2013**, *42*, 1440−1459.
(4) Kaim, W.; Schwederski, B. Non-innocent ligands in bioinorganic chemistry—An overview. *Coord. Chem. Rev.* **2010**, *254*, 1580−1588.
(5) Chirik, P. J.; Wieghardt, K. Radical ligands confer nobility on base-metal catalysts. *Science* **2010**, *327*, 794.
(6) Praneeth, V. K. K.; Ringenberg, M. R.; Ward, T. R. Redox-active ligands in catalysis. *Angew. Chem., Int. Ed.* **2012**, *51*, 10228−10234.
(7) van der Vlugt, J. I. Cooperative catalysis with first-row late transition metals. *Eur. J. Inorg. Chem.* **2012**, *2012*, 363−375.
(8) Lyaskovskyy, V.; de Bruin, B. Redox non-innocent ligands: Versatile new tools to control catalytic reactions. *ACS Catal.* **2012**, *2*, 270−279.
(9) Alig, L.; Fritz, M.; Schneider, S. First-row transition metal (de)hydrogenation catalysis based on functional pincer ligands. *Chem. Rev.* **2019**, *119*, 2681−2751.
(10) Berben, L. A.; de Bruin, B.; Heyduk, A. F. Non-innocent ligands. *Chem. Commun.* **2015**, *51*, 1553−1554.
(11) van der Vlugt, J. I. Radical-type reactivity and catalysis by single-electron transfer to or from redox-active ligands. *Chem. - Eur. J.* **2019**, *25*, 2651−2662.
(12) Jacquet, J.; Desage-El Murr, M.; Fensterbank, L. Metal-promoted coupling reactions implying ligand-based redox changes. *ChemCatChem* **2016**, *8*, 3310−3316.
(13) Allgeier, A. M.; Mirkin, C. A. Ligand design for electrochemically controlling stoichiometric and catalytic reactivity of transition metals. *Angew. Chem., Int. Ed.* **1998**, *37*, 894−908.
(14) Broere, D. L. J.; Plessius, R.; van der Vlugt, J. I. New avenues for ligand-mediated processes - expanding metal reactivity by the use of redox-active catechol, o-aminophenol and o-phenylenediamine ligands. *Chem. Soc. Rev.* **2015**, *44*, 6886−6915.
(15) Balch, A. L.; Holm, R. H. Complete electron-transfer series of the [M-N_4] type. *J. Am. Chem. Soc.* **1966**, *88*, 5201−5209.
(16) Kruger, H. J.; Peng, G.; Holm, R. H. Low-potential nickel(III,II) complexes: new systems based on tetradentate amidate-thiolate ligands and the influence of ligand structure on potentials in relation to the nickel site in [NiFe]-hydrogenases. *Inorg. Chem.* **1991**, *30*, 734−742.
(17) Chaudhuri, P.; Hess, M.; Müller, J.; Hildenbrand, K.; Bill, E.; Weyhermüller, T.; Wieghardt, K. Aerobic oxidation of primary alcohols (including methanol) by copper(II)- and zinc(II)-phenoxyl radical catalysts. *J. Am. Chem. Soc.* **1999**, *121*, 9599−9610.
(18) Holm, R. H. Nickel(II) complexes. I. Spectra of tricyclic Schiff base complexes of nickel(II) and copper(II). *J. Am. Chem. Soc.* **1960**, *82*, 5632−5636.
(19) Thomas, F. Ligand-centered oxidative chemistry in sterically hindered salen complexes: an interesting case with nickel. *Dalton Trans* **2016**, *45*, 10866−10877.
(20) Ciccione, J.; Leconte, N.; Luneau, D.; Philouze, C.; Thomas, F. Geometric and electronic structures of nickel(II) complexes of redox noninnocent tetradentate phenylenediamine ligands. *Inorg. Chem.* **2016**, *55*, 649−665.
(21) Mitra, K. N.; Choudhury, S.; Castineiras, A.; Goswami, S. Chemistry of ruthenium(II) complexes of N-substituted 1,2-benzoquinone diimines. Synthesis, structure and redox properties. *J. Chem. Soc., Dalton Trans.* **1998**, 2901−2906.
(22) Skara, G.; Pinter, B.; Geerlings, P.; De Proft, F. Revealing the thermodynamic driving force for ligand-based reductions in quinoids; conceptual rules for designing redox active and non-innocent ligands. *Chem. Sci.* **2015**, *6*, 4109−4117.
(23) Fry, N. L.; Rose, M. J.; Nyitray, C.; Mascharak, P. K. Facile ligand oxidation and ring nitration in ruthenium complexes derived from a ligand with dicarboxamide-N and phosphine-P donors. *Inorg. Chem.* **2008**, *47*, 11604−11610.
(24) Majumdar, P.; Falvello, L. R.; Tomás, M.; Goswami, S. A novel dinuclear ruthenium complex bridged through a substituted phenazine ligand formed by ruthenium-promoted oxidative assembly of 1,3-diaminobenzene. *Chem. - Eur. J.* **2001**, *7*, 5222−5228.
(25) Metcalfe, R. A.; Lever, A. B. P. Tetraammineruthenium(II) and -ruthenium(III) complexes of *o*-benzoquinone diimine and their redox series. *Inorg. Chem.* **1997**, *36*, 4762−4771.
(26) Santana da Silva, R.; Gorelsky, S. I.; Dodsworth, E. S.; Tfouni, E.; Lever, A. B. P. Synthesis, spectral and redox properties of tetraammine dioxolene ruthenium complexes. *J. Chem. Soc., Dalton Trans.* **2000**, 4078−4088.
(27) Shaw, J. L.; Wolowska, J.; Collison, D.; Howard, J. A. K.; McInnes, E. J. L.; McMaster, J.; Blake, A. J.; Wilson, C.; Schroeder, M. Redox Non-innocence of Thioether Macrocycles: Elucidation of the Electronic Structures of Mononuclear Complexes of Gold(II) and Silver(II). *J. Am. Chem. Soc.* **2006**, *128*, 13827−13839.
(28) Stephen, E.; Huang, D.; Shaw, J. L.; Blake, A. J.; Collison, D.; Davies, E. S.; Edge, R.; Howard, J. A. K.; McInnes, E. J. L.; Wilson, C.; Wolowska, J.; McMaster, J.; Schroder, M. Redox non-innocence of thioether crowns: spectroelectrochemistry and electronic structure of formal nickel(III) complexes of aza-thioether macrocycles. *Chem. - Eur. J.* **2011**, *17*, 10246−10258.
(29) Martinez-Alanis, P. R.; Sanchez Eguia, B. N.; Ugalde-Saldivar, V. M.; Regla, I.; Demare, P.; Aullon, G.; Castillo, I. Copper versus thioether-centered oxidation: mechanistic insights into the non-

DOI: 10.1021/acs.inorgchem.9b01675
Inorg. Chem. 2019, 58, 12756−12774

innocent redox behavior of tripodal benzimidazolylaminothioether ligands. *Chem. - Eur. J.* **2013**, *19*, 6067−6079.
(30) Inoue, S.; Mitsuhashi, M.; Ono, T.; Yan, Y.-N.; Kataoka, Y.; Handa, M.; Kawamoto, T. Photo- and electrocatalytic hydrogen production using valence isomers of N_2S_2-type nickel complexes. *Inorg. Chem.* **2017**, *56*, 12129.
(31) Durgaprasad, G.; Luna, J. A.; Spielvogel, K. D.; Haas, C.; Shaw, S. K.; Daly, S. R. Ru(II) complexes with a chemical and redox-active S_2N_2 ligand: Structures, electrochemistry, and metal-ligand cooperativity. *Organometallics* **2017**, *36*, 4020−4031.
(32) Bayer, E.; Breitmaier, E. Umlagerung und komplexbildung des glyoxal-bis-[2-mercapto-anils] und anderer mercaptoanile. *Chem. Ber.* **1968**, *101*, 1579−1593.
(33) Chłopek, K.; Bothe, E.; Neese, F.; Weyhermüller, T.; Wieghardt, K. Molecular and electronic structures of tetrahedral complexes of nickel and cobalt containing N,N'-disubstituted, bulky *o*-diiminobenzosemiquinonate(1-) π-radical ligands. *Inorg. Chem.* **2006**, *45*, 6298−6307.
(34) Rosenkoetter, K. E.; Wojnar, M. K.; Charette, B. J.; Ziller, J. W.; Heyduk, A. F. Hydrogen-atom noninnocence of a tridentate [SNS] pincer ligand. *Inorg. Chem.* **2018**, *57*, 9728−9737.
(35) Singh, J.; Hundal, G.; Gupta, R. Studies on nickel(II) complexes with amide-based ligands: Syntheses, structures, electrochemistry and oxidation chemistry. *Eur. J. Inorg. Chem.* **2008**, *2008*, 2052−2063.
(36) Stavropoulos, P.; Carrie, M.; Muetterties, M. C.; Holm, R. H. Reaction sequence related to that of carbon monoxide dehydrogenase (acetyl coenzyme A synthase): thioester formation mediated at structurally defined nickel centers. *J. Am. Chem. Soc.* **1990**, *112*, 5385−5387.
(37) Hong, D.; Tsukakoshi, Y.; Kotani, H.; Ishizuka, T.; Ohkubo, K.; Shiota, Y.; Yoshizawa, K.; Fukuzumi, S.; Kojima, T. Mechanistic insights into homogeneous electrocatalytic and photocatalytic hydrogen evolution catalyzed by high-spin Ni(II) complexes with S_2N_2-type tetradentate ligands. *Inorg. Chem.* **2018**, *57*, 7180−7190.
(38) Jain, R.; Mamun, A. A.; Buchanan, R. M.; Kozlowski, P. M.; Grapperhaus, C. A. Ligand-assisted metal-centered electrocatalytic hydrogen evolution upon reduction of a bis(thiosemicarbazonato)-Ni(II) complex. *Inorg. Chem.* **2018**, *57*, 13486−13493.
(39) Smith, C. I.; Crayston, J. A.; Hay, R. W. Reduction of carbon dioxide by nickel macrocyclic catalysts adsorbed on a mercury electrode or a copper rotating disc electrode. *J. Chem. Soc., Dalton Trans.* **1993**, 3267−3269.
(40) Connelly, N. G.; Geiger, W. E. Chemical redox agents for organometallic chemistry. *Chem. Rev.* **1996**, *96*, 877−910.
(41) Souverain, D.; Leborgne, A.; Sauvet, G.; Sigwalt, P. Polymerizations of ethylenic monomers initiated by superacids—II: complexation of some trifluoromethanesulphonates by their conjugate acid. *Eur. Polym. J.* **1980**, *16*, 861−865.
(42) Foropoulos, J., Jr; DesMarteau, D. D. Synthesis, properties, and reactions of bis((trifluoromethyl)sulfonyl)imide, $(CF_3SO_2)_2NH$. *Inorg. Chem.* **1984**, *23*, 3720−3723.
(43) Vij, A.; Zheng, Y. Y.; Kirchmeier, R. L.; Shreeve, J. n. M. Electrophilic addition and substitution reactions of bis-((trifluoromethyl)sulfonyl)amide and its N-chloro derivative. *Inorg. Chem.* **1994**, *33*, 3281−3288.
(44) Lecarme, L.; Chiang, L.; Philouze, C.; Jarjayes, O.; Storr, T.; Thomas, F. Detailed geometric and electronic structures of a one-electron-oxidized Ni salophen complex and its amido derivatives. *Eur. J. Inorg. Chem.* **2014**, *2014*, 3479−3487.
(45) Enamullah, M.; Makhloufi, G.; Ahmed, R.; Joy, B. A.; Islam, M. A.; Padula, D.; Hunter, H.; Pescitelli, G.; Janiak, C. Synthesis, X-ray, and Spectroscopic Study of Dissymmetric Tetrahedral Zinc(II) Complexes from Chiral Schiff Base Naphthaldiminate Ligands with Apparent Exception to the ECD Exciton Chirality. *Inorg. Chem.* **2016**, *55*, 6449−6464.
(46) Drago, R. S. *Physical methods for chemists*, 2nd ed.; Surfside Scientific Publishers: Gainesville, FL, 1992.
(47) Girolami, G. S.; Rauchfuss, T. B.; Angelici, R. J. *Synthesis and technique in inorganic chemistry: A laboratory manual*, 3rd ed.; University Science Books: Sausalito, CA, 1999.
(48) West, A. R. *Solid state chemistry and its applications*; John Wiley & Sons: 2014.
(49) Chmielewski, P. J.; Latos-Grażyński, L. EPR and 2H NMR studies on the oxidation of nickel(II) tetraphenylcarbaporphyrin to form novel organometallic nickel(III) complexes. *Inorg. Chem.* **1997**, *36*, 840−845.
(50) Ottenwaelder, X.; Ruiz-García, R.; Blondin, G.; Carasco, R.; Cano, J.; Lexa, D.; Journaux, Y.; Aukauloo, A. From metal to ligand electroactivity in nickel(II) oxamato complexes. *Chem. Commun.* **2004**, 504−505.
(51) Krueger, H. J.; Holm, R. H. Stabilization of nickel(III) in a classical N_2S_2 coordination environment containing anionic sulfur. *Inorg. Chem.* **1987**, *26*, 3645−3647.
(52) De Castro, B.; Freire, C. EPR and electrochemical study of nickel(III) complexes of bis(3,5-dichlorosalicylaldehyde) o-phenylenediimine. Evidence for adduct formation with pyridines. *Inorg. Chem.* **1990**, *29*, 5113−5119.
(53) Lyons, C. T.; Stack, T. D. P. Recent advances in phenoxyl radical complexes of salen-type ligands as mixed-valent galactose oxidase models. *Coord. Chem. Rev.* **2013**, *257*, 528−540.
(54) Evangelio, E.; Ruiz-Molina, D. Valence tautomerism: New challenges for electroactive ligands. *Eur. J. Inorg. Chem.* **2005**, *2005*, 2957−2971.
(55) Zima, A. M.; Lyakin, O. Y.; Ottenbacher, R. V.; Bryliakov, K. P.; Talsi, E. P. Iron-catalyzed enantioselective epoxidations with various oxidants: Evidence for different active species and epoxidation mechanisms. *ACS Catal.* **2017**, *7*, 60−69.
(56) Himmel, H.-J. Valence tautomerism in copper coordination chemistry. *Inorg. Chim. Acta* **2018**, *481*, 56−68.
(57) Lee, H.; Börgel, J.; Ritter, T. Carbon-fluorine reductive elimination from nickel(III) complexes. *Angew. Chem., Int. Ed.* **2017**, *56*, 6966−6969.
(58) Rotthaus, O.; Jarjayes, O.; Thomas, F.; Philouze, C.; Perez Del Valle, C.; Saint-Aman, E.; Pierre, J. L. Fine tuning of the oxidation locus, and electron transfer, in nickel complexes of pro-radical ligands. *Chem. - Eur. J.* **2006**, *12*, 2293−2302.
(59) Rotthaus, O.; Jarjayes, O.; Perez Del Valle, C.; Philouze, C.; Thomas, F. A versatile electronic hole in one-electron oxidized Ni^{II} bis-salicylidene phenylenediamine complexes. *Chem. Commun.* **2007**, 4462−4464.
(60) Storr, T.; Wasinger, E. C.; Pratt, R. C.; Stack, T. D. P. The geometric and electronic structure of a one-electron-oxidized nickel(II) bis(salicylidene)diamine complex. *Angew. Chem., Int. Ed.* **2007**, *46*, 5198−5201.
(61) Chiang, L.; Herasymchuk, K.; Thomas, F.; Storr, T. Influence of electron-withdrawing substituents on the electronic structure of oxidized Ni and Cu salen complexes. *Inorg. Chem.* **2015**, *54*, 5970−5980.
(62) Kunert, R.; Philouze, C.; Jarjayes, O.; Thomas, F. Stable M(II)-radicals and nickel(III) complexes of a bis(phenol) N-heterocyclic carbene chelated to group 10 metal ions. *Inorg. Chem.* **2019**, *58*, 8030−8044.
(63) Ghosh, M.; Weyhermüller, T.; Wieghardt, K. Electronic structure of the members of the electron transfer series [NiL]z (z = 3+, 2+, 1+, 0) and $[NiL(X)]_n$ (X = Cl, CO, $P(OCH_3)_3$) species containing a tetradentate, redox-noninnocent, Schiff base macrocyclic ligand L: an experimental and density functional theoretical study. *Dalton Trans* **2010**, *39*, 1996−2007.
(64) Rotthaus, O.; Labet, V.; Philouze, C.; Jarjayes, O.; Thomas, F. Pseudo-octahedral Schiff base nickel(II) complexes: does single oxidation always lead to the nickel(III) valence tautomer? *Eur. J. Inorg. Chem.* **2008**, *2008*, 4215−4224.
(65) Ferentinos, E.; Raptopoulou, C. P.; Psycharis, V.; Terzis, A.; Krzystek, J.; Kyritsis, P. Magnetostructural correlations in S = 1 trans-$[Ni\{(OPPh_2)(EPPh_2)N\}_2(dmso)_2]$, E = S, Se, and related complexes. *Polyhedron* **2018**, *151*, 177−184.

DOI: 10.1021/acs.inorgchem.9b01675
Inorg. Chem. 2019, 58, 12756−12774

(66) Schweinfurth, D.; Krzystek, J.; Schapiro, I.; Demeshko, S.; Klein, J.; Telser, J.; Ozarowski, A.; Su, C.-Y.; Meyer, F.; Atanasov, M.; Neese, F.; Sarkar, B. Electronic structures of octahedral Ni(II) complexes with "click" derived triazole ligands: A combined structural, magnetometric, spectroscopic, and theoretical study. *Inorg. Chem.* **2013**, *52*, 6880−6892.
(67) Krzystek, J.; Park, J.-H.; Meisel, M. W.; Hitchman, M. A.; Stratemeier, H.; Brunel, L.-C.; Telser, J. EPR spectra from "EPR-silent" species: High-frequency and high-field EPR spectroscopy of pseudotetrahedral complexes of nickel(II). *Inorg. Chem.* **2002**, *41*, 4478−4487.
(68) Arumugam, K.; Shaw, M. C.; Mague, J. T.; Bill, E.; Sproules, S.; Donahue, J. P. Long-Range Spin Coupling: A Tetraphosphine-Bridged Palladium Dimer. *Inorg. Chem.* **2011**, *50*, 2995−3002.
(69) Dunn, T. J.; Chiang, L.; Ramogida, C. F.; Hazin, K.; Webb, M. I.; Katz, M. J.; Storr, T. Class III Delocalization and Exciton Coupling in a Bimetallic Bis-ligand Radical Complex. *Chem. - Eur. J.* **2013**, *19*, 9606−9618.
(70) Herebian, D.; Wieghardt, K. E.; Neese, F. Analysis and interpretation of metal-radical coupling in a series of square planar nickel complexes: correlated ab initio and density functional investigation of $[Ni(LISQ)_2]$ (LISQ = 3,5-di-tert-butyl-*o*-diimino-benzosemiquinonate (1-)). *J. Am. Chem. Soc.* **2003**, *125*, 10997−11005.
(71) Mavros, M. G.; Tsuchimochi, T.; Kowalczyk, T.; McIsaac, A.; Wang, L.-P.; Van Voorhis, T. What can density functional theory tell us about artificial catalytic water splitting? *Inorg. Chem.* **2014**, *53*, 6386−6397.
(72) Cramer, C. J.; Truhlar, D. G. Density functional theory for transition metals and transition metal chemistry. *Phys. Chem. Chem. Phys.* **2009**, *11*, 10757−10816.
(73) Sarangi, R.; DeBeer George, S.; Rudd, D. J.; Szilagyi, R. K.; Ribas, X.; Rovira, C.; Almeida, M.; Hodgson, K. O.; Hedman, B.; Solomon, E. I. Sulfur K-Edge X-ray Absorption Spectroscopy as a Probe of Ligand-Metal Bond Covalency: Metal vs Ligand Oxidation in Copper and Nickel Dithiolene Complexes. *J. Am. Chem. Soc.* **2007**, *129*, 2316−2326.
(74) Glaser, T.; Hedman, B.; Hodgson, K. O.; Solomon, E. I. Ligand K-Edge X-ray Absorption Spectroscopy: A Direct Probe of Ligand-Metal Covalency. *Acc. Chem. Res.* **2000**, *33*, 859−868.
(75) Szilagyi, R. K.; Lim, B. S.; Glaser, T.; Holm, R. H.; Hedman, B.; Hodgson, K. O.; Solomon, E. I. Description of the ground state wave functions of Ni dithiolenes using sulfur K-edge X-ray absorption spectroscopy. *J. Am. Chem. Soc.* **2003**, *125*, 9158−9169.
(76) Sproules, S.; Wieghardt, K. Dithiolene radicals: Sulfur K-edge X-ray absorption spectroscopy and Harry's intuition. *Coord. Chem. Rev.* **2011**, *255*, 837−860.
(77) Solomon, E. I.; Hedman, B.; Hodgson, K. O.; Dey, A.; Szilagyi, R. K. Ligand K-edge X-ray absorption spectroscopy: covalency of ligand-metal bonds. *Coord. Chem. Rev.* **2005**, *249*, 97−129.
(78) Dey, S.; Wayland, B. B.; Zdilla, M. J. Solution and solid state properties for low-spin cobalt(II) dibenzotetramethyltetraaza[14]-annulene [(tmtaa)CoII] and the monopyridine complex. *Inorg. Chem.* **2019**, *58*, 1224−1233.
(79) *Macromolecular Crystallography, Part A*; Otwinowski, Z., Minor, W., Eds.; Academic Press: New York, 1997; Vol. *276*.
(80) *Bruker SADABS v.2.03*; Bruker AXS Inc.: Madison, WI, 2001.
(81) Dolomanov, O. V.; Bourhis, L. J.; Gildea, R. J.; Howard, J. A. K.; Puschmann, H. OLEX2: a complete structure solution, refinement and analysis program. *J. Appl. Crystallogr.* **2009**, *42*, 339−341.
(82) Spek, A. L. PLATON SQUEEZE: a tool for the calculation of the disordered solvent contribution to the calculated structure factors. *Acta Crystallogr., Sect. C: Struct. Chem.* **2015**, *71*, 9−18.
(83) Sheldrick, G. M. SHELXT-Integrated space-group and crystal-structure determination. *Acta Crystallogr., Sect. A: Found. Adv.* **2015**, *71*, 3−8.
(84) Sheldrick, G. M. Crystal structure refinement with SHELXL. *Acta Crystallogr., Sect. C: Struct. Chem.* **2015**, *71*, 3−8.
(85) Macrae, C. F.; Bruno, I. J.; Chisholm, J. A.; Edgington, P. R.; McCabe, P.; Pidcock, E.; Rodriguez-Monge, L.; Taylor, R.; van de Streek, J.; Wood, P. A. Mercury CSD 2.0 - new features for the visualization and investigation of crystal structures. *J. Appl. Crystallogr.* **2008**, *41*, 466−470.
(86) Stoll, S.; Schweiger, A. EasySpin, a comprehensive software package for spectral simulation and analysis in EPR. *J. Magn. Reson.* **2006**, *178*, 42−55.
(87) Misra, S. K. *Multifrequency Electron Paramagnetic Resonance: Data and Techniques*; John Wiley & Sons: 2014.
(88) Donahue, C. M.; McCollom, S. P.; Forrest, C. M.; Blake, A. V.; Bellott, B. J.; Keith, J. M.; Daly, S. R. Impact of coordination geometry, bite angle, and trans influence on metal-ligand covalency in phenyl-substituted phosphine complexes of Ni and Pd. *Inorg. Chem.* **2015**, *54*, 5646−5659.
(89) Donahue, C. M.; Lezama Pacheco, J. S.; Keith, J. M.; Daly, S. R. Sulfur K-edge X-ray absorption spectroscopy and time-dependent density functional theory of arsenic dithiocarbamates. *Dalton Trans* **2014**, *43*, 9189−9201.
(90) Blake, A. V.; Wei, H.; Lee, K.; Donahue, C. M.; Keith, J. M.; Daly, S. R. Solution and solid-state ligand K-edge XAS studies of $PdCl_2$ diphosphine complexes with phenyl and cyclohexyl substituents. *Eur. J. Inorg. Chem.* **2018**, *2018*, 2267−2276.
(91) Blake, A. V.; Wei, H.; Donahue, C. M.; Lee, K.; Keith, J. M.; Daly, S. R. Solid energy calibration standards for P K-edge XANES: electronic structure analysis of PPh_4Br. *J. Synchrotron Radiat.* **2018**, *25*, 529−536.
(92) Lee, K.; Wei, H.; Blake, A. V.; Donahue, C. M.; Keith, J. M.; Daly, S. R. Ligand K-edge XAS, DFT, and TDDFT analysis of pincer linker variations in Rh(I) PNP complexes: reactivity insights from electronic structure. *Dalton Trans* **2016**, *45*, 9774−9785.
(93) Lee, K.; Wei, H.; Blake, A. V.; Donahue, C. M.; Keith, J. M.; Daly, S. R. Measurement of diphosphine σ-donor and π-acceptor properties in d^0 titanium complexes using ligand K-edge XAS and TDDFT. *Inorg. Chem.* **2018**, *57*, 10277−10286.
(94) Ravel, B.; Newville, M. ATHENA, ARTEMIS, HEPHAESTUS: data analysis for X-ray absorption spectroscopy using IFEFFIT. *J. Synchrotron Radiat.* **2005**, *12*, 537−541.
(95) Hedman, B.; Frank, P.; Penner-Hahn, J. E.; Roe, A. L.; Hodgson, K. O.; Carlson, R. M. K.; Brown, G.; Cerino, J.; Hettel, R.; Troxel, T.; Winick, H.; Yang, J. Sulfur K-edge X-ray absorption studies using the 54-pole wiggler at SSRL in undulator mode. *Nucl. Instrum. Methods Phys. Res., Sect. A* **1986**, *246*, 797−800.

DOI: 10.1021/acs.inorgchem.9b01675
Inorg. Chem. 2019, 58, 12756−12774